THE ASTRONOMICAL JOURNAL, 118:1738–1758, 1999 October

THE GIANT, HORIZONTAL, AND ASYMPTOTIC BRANCHES OF GALACTIC GLOBULAR CLUSTERS. I. THE CATALOG, PHOTOMETRIC OBSERVABLES, AND FEATURES

F. R. FERRARO,[1,2] M. MESSINEO,[1] F. FUSI PECCI,[1,3] M. A. DE PALO,[4] O. STRANIERO,[5] A. CHIEFFI,[6] AND M. LIMONGI[7]
Received 1999 January 1; accepted 1999 June 8

ABSTRACT

A catalog including a set of the most recent color-magnitude diagrams (CMDs) is presented for a sample of 61 Galactic globular clusters (GGCs). We used this database to perform a homogeneous systematic analysis of the evolved sequences (namely, the red giant branch [RGB], horizontal branch [HB], and asymptotic giant branch [AGB]). Based on this analysis, we present (1) a new procedure to measure the level of the zero-age horizontal branch (V_{ZAHB}) and a homogeneous set of distance moduli obtained by adopting the HB as standard candle; (2) an independent estimate for RGB metallicity indicators and new calibrations of these parameters in terms of both spectroscopic ($[Fe/H]_{CG97}$) and global metallicity ([M/H], including also the α-element enhancement), such that the set of equations presented can be used to simultaneously derive a *photometric* estimate of the metal abundance and the reddening from the morphology and the location of the RGB in the $(V, B-V)$ CMD; and (3) the location of the RGB bump (in 47 GGCs) and the AGB bump (in nine GGCs). The dependence of these features on metallicity is discussed. We find that by using the latest theoretical models and the new metallicity scales, the earlier discrepancy between theory and observations ($\sim$0.4 mag) completely disappears.

Key words: globular clusters: general — stars: evolution — stars: horizontal-branch — stars: Population II

1. INTRODUCTION

Stellar evolutionary models are often used to infer relevant properties of the Galaxy and the early universe; for this reason the check of their adequacy and accuracy can be regarded as a pivotal project of modern astrophysical research (Renzini & Fusi Pecci 1988). The advent of the charge-coupled device (CCD) and, more recently, the availability of the *Hubble Space Telescope*, supported by the modern highly powerful software for photometric data analysis in crowded fields, have greatly enhanced the possibility of using the Galactic globular clusters (GGCs) as the ideal laboratory to test the stellar evolution theories.

Within this framework, we started a long-term project devoted to carrying out a detailed quantitative analysis of the evolved sequences (namely, the red giant branch, horizontal branch, and asymptotic giant branch, hereafter RGB, HB, and AGB, respectively) in the color-magnitude diagram (CMD) of GGCs. The methodological approach of our study has been presented in a series of papers concerning the photometry of wide samples of stars in a selected set of GGCs (see, e.g., Ferraro et al. 1990, 1991, 1992a; Ferraro, Fusi Pecci, & Buonanno 1992b; Ferraro et al. 1993a, 1994, 1995b, 1997a; Buonanno et al. 1994). Some results on specific sequences can be found in Fusi Pecci et al. (1990, hereafter F90) and Ferraro (1992) (for the RGB), Fusi Pecci et al. (1992, 1993), Buonanno et al. (1997), and Ferraro et al. (1997b, 1998) (for the HB), and Ferraro, Fusi Pecci, & Bellazzini (1995a) and Ferraro et al. (1993b, 1997c, 1999) (for the blue stragglers).

This is the first in a series of papers devoted to studying the characteristics of the RGB, HB, and AGB for the widest available sample of GGCs with *good BV* photometry. In this paper we present the catalog of the most recent CMDs for GGCs. From these we derive photometric observables along the RGB, HB, and AGB that yield new, independent measures of some peculiar features (e.g., the so-called RGB bump). The study will soon be extended in a second paper to explore the existence and extent of mixing processes (such as semiconvection and overshooting) in the stellar interiors. These processes have a direct impact on the duration of the post–helium-flash phases (HB and AGB) and, in turn, on the use of population ratios to determine one of the fundamental cosmological parameters, the helium abundance (Y_p), via the so-called R-method (Iben 1968; Buzzoni et al. 1983).

The paper is organized as follows: In § 2, we present the complete database used in our analysis, which includes CMDs for 61 GGCs, while § 3 is devoted to a discussion of the metallicity scales. Section 4 reports the basic assumptions of the theoretical models adopted throughout the paper. In § 5, we present a new procedure (based on the use of synthetic CMDs) to measure the level of the zero-age horizontal branch (ZAHB) (frequently adopted as standard luminosity reference). Section 6 deals with the presentation of new homogenous determinations of the RGB morphological parameters, their calibrations in terms of the adopted spectroscopic and global metallicities, and the determination of the RGB bump luminosity and its comparison with theoretical expectations. Similarly, § 7 is devoted to the study of the photometric properties of the AGB bump. Finally, in § 8, after adopting different self-consistent distance scales, we report the results of a global

[1] Osservatorio Astronomico di Bologna, via Zamboni 33, I-40126 Bologna, Italy.
[2] European Southern Observatory, Karl-Schwarzschild-Strasse 2, D-85748 Garching bei Munchen, Germany.
[3] Stazione Astronomica di Cagliari, I-09012 Capoterra, Italy.
[4] Dipartimento di Astronomia, Università di Bologna, I-40126 Bologna, Italy.
[5] Osservatorio Astronomico di Collurania, via M. Vaggini, I-64100 Teramo, Italy.
[6] Istituto di Astrofisica Spaziale del CNR, C.P. 67, I-00044 Frascati, Italy.
[7] Osservatorio Astronomico di Monte Porzio, I-00040 Monte Porzio Catone, Italy.

TABLE 1

THE ADOPTED DATABASE

Name (1)	$[Fe/H]_{Z85}$ (2)	$[Fe/H]_{CG97}$ (3)	[M/H] (4)	$E(B-V)$ (5)	References (6)
NGC 104	−0.71	−0.70	−0.59	0.04	Montegriffo et al. 1995; Hesser et al. 1987
NGC 288	−1.40	−1.07	−0.85	0.03	Bergbusch 1993; Buonanno et al. 1984
NGC 362	−1.28	−1.15	−0.99	0.05	Harris 1982
NGC 1261.....	−1.31	−1.09	−0.89	0.02	Ferraro et al. 1993a
NGC 1466.....	−1.85	−1.64	−1.44	0.09	Walker 1992a
NGC 1841.....	−2.20	−2.11	−1.91	0.18	Walker 1990
NGC 1851.....	−1.29	−1.08	−0.88	0.02	Walker 1992b
NGC 1904.....	−1.69	−1.37	−1.22	0.01	Ferraro et al. 1992a
NGC 2419.....	−2.10	−1.97	−1.77	0.03	Christian & Heasley 1988
NGC 2808.....	−1.37	−1.15	−0.95	0.23	Ferraro et al. 1990
NGC 3201.....	−1.61	−1.23	−1.03	0.21	Covino & Ortolani 1997
NGC 4147.....	−1.80	−1.58	−1.38	0.02	Sandage & Walker 1955
NGC 4372.....	−2.08	−1.94	−1.74	0.45	Brocato et al. 1996
NGC 4590.....	−2.09	−1.99	−1.81	0.04	Walker 1994
NGC 4833.....	−1.86	−1.58	−1.27	0.33	Momany 1996
NGC 5053.....	−2.58	−2.51	−2.31	0.03	Sarajedini & Milone 1995
NGC 5272.....	−1.66	−1.34	−1.16	0.01	Buonanno et al. 1994; Ferraro et al. 1997a, 1997c
NGC 5286.....	−1.79	−1.57	−1.37	0.24	Brocato et al. 1996
NGC 5466.....	−2.22	−2.14	−1.94	0.00	Buonanno, Corsi, & Fusi Pecci 1985
NGC 5694.....	−1.91	−1.72	−1.52	0.09	Ortolani & Gratton 1990
NGC 5824.....	−1.85	−1.64	−1.44	0.14	Brocato et al. 1996
NGC 5897.....	−1.68	−1.59	−1.44	0.08	Ferraro et al. 1992b
NGC 5904.....	−1.40	−1.11	−0.90	0.03	Buonanno, Corsi, & Fusi Pecci 1981; Brocato, Castellani, & Ripepi 1995
NGC 5927.....	−0.31	−0.46	−0.37	0.47	Samus et al. 1995
NGC 6093.....	−1.64	−1.41	−1.21	0.18	Brocato et al. 1998
NGC 6121.....	−1.33	−1.19	−0.94	0.36	Lee 1977
NGC 6171.....	−0.99	−0.87	−0.70	0.33	Ferraro et al. 1991
NGC 6205.....	−1.65	−1.39	−1.18	0.02	Paltrinieri et al. 1998
NGC 6218.....	−1.61	−1.37	−1.17	0.17	Brocato et al. 1996
NGC 6229.....	−1.54	−1.30	−1.10	0.01	Carney, Fullton, Trammell 1991; Borissova et al. 1997
NGC 6254.....	−1.60	−1.41	−1.25	0.28	Harris, Racine, & de Roux 1976
NGC 6266.....	−1.28	−1.07	−0.87	0.47	Brocato et al. 1996
NGC 6333.....	−1.78	−1.56	−1.36	0.36	Janes & Heasley 1991
NGC 6341.....	−2.24	−2.16	−1.95	0.02	Buonanno et al. 1985
NGC 6352.....	−0.51	−0.64	−0.50	0.21	Bordoni 1995
NGC 6366.....	−0.99	−0.87	−0.70	0.69	Pike 1976
NGC 6397.....	−1.91	−1.82	−1.65	0.18	Kaluzny 1997
NGC 6440.....	−0.34	−0.49	−0.40	1.09	Ortolani, Barbuy, & Bica 1994a
NGC 6528.....	−0.23	−0.38	−0.31	0.62	Ortolani et al. 1995
NGC 6535.....	−1.75	−1.53	−1.33	0.32	Sarajedini 1994a
NGC 6553.....	−0.29	−0.44	−0.36	0.84	Ortolani et al. 1995
NGC 6584.....	−1.54	−1.30	−1.10	0.11	Sarajedini & Forrester 1995
NGC 6637.....	−0.59	−0.68	−0.55	0.17	Ferraro et al. 1994
NGC 6652.....	−0.99	−0.87	−0.70	0.09	Ortolani, Bica, & Barbuy 1994b
NGC 6681.....	−1.51	−1.27	−1.07	0.07	Brocato et al. 1996
NGC 6712.....	−1.01	−0.88	−0.71	0.46	Cudworth 1988
NGC 6717.....	−1.32	−1.10	−0.90	0.21	Brocato et al. 1996
NGC 6752.....	−1.54	−1.42	−1.21	0.04	Buonanno et al. 1986
NGC 6809.....	−1.82	−1.61	−1.41	0.07	Desidera 1996
NGC 6838.....	−0.58	−0.70	−0.49	0.25	Cudworth 1985
NGC 6934.....	−1.54	−1.30	−1.10	0.11	Brocato et al. 1996
NGC 6981.....	−1.54	−1.30	−1.10	0.05	Brocato et al. 1996
NGC 7006.....	−1.59	−1.35	−1.15	0.05	Buonanno et al. 1991
NGC 7078.....	−2.17	−2.12	−1.91	0.09	Buonanno et al. 1985
NGC 7099.....	−2.13	−1.91	−1.71	0.03	Bergbusch 1996
NGC 7492.....	−1.51	−1.27	−1.07	0.00	Buonanno et al. 1987
IC 4499	−1.50	−1.26	−1.06	0.24	Ferraro et al. 1995b
Rup 106	−1.90	−1.70	−1.50	0.21	Buonanno et al. 1993
Arp 2.....	−1.85	−1.64	−1.44	0.11	Buonanno et al. 1995a
Ter 7	−0.49	−0.64	−0.52	0.06	Buonanno et al. 1995b
Ter 8	−1.81	−1.60	−1.40	0.14	Ortolani & Gratton 1990

comparison with the absolute quantities predicted by the theoretical models.

2. THE DATABASE

After reviewing the published literature on CMDs for GGCs, it is a little surprising to discover that the number of GGCs for which a modern (CCD) CMD is available is less than 50% of the whole cluster population in the Galaxy. This percentage is further decreased if one restricts the sample, as we did, to only the clusters with CMDs of sufficient photometric accuracy, population size, and degree of completeness down the HB blue extension.

Moreover, since we want to perform homogenous independent measures and star counts over the whole CMD, we included in our final sample only the GGCs whose data sets (star magnitudes and positions) were available as electronic files (upon direct request to the author or scanned from the reference paper). In the final choice, we dropped CMDs with inadequate completeness checks and usually adopted the most recent papers. If different CMDs of comparable quality were available for the same cluster, after carefully checking the radial extension of the samples and their photometric compatibility, we merged them in order to increase the statistical significance of the adopted sample.

The final sample of GGCs whose CMDs have been classified as "good enough" includes 61 objects, for which we list in Table 1 the name, the metallicity in the considered scales (see next section), the reddening from a recent compilation (Harris 1996), and the reference for the adopted CMD. Admittedly, the selected sample is quite heterogeneous in many respects: the cluster light sampling, the photometric accuracy, and the absolute calibration actually achieved by each individual photometry. However, no attempt has been made at this level to rank the clusters on the basis of the overall quality of the CMD. In the next paper, specifically devoted to presentation and discussion of the population ratios, a more significative classification will be performed on the basis of the global population of bright stars (AGB + HB + RGB) sampled in each cluster.

3. METALLICITY SCALES

3.1. *The Zinn Scale*

One of the most widely used scales for the metal abundance in GGCs was proposed during the early 1980s by Zinn and collaborators (Zinn 1980; Zinn & West 1984; Zinn 1985, hereafter Z85; Armandroff & Zinn 1988). This scale was obtained from the integrated light parameter Q_{39}, tied to the Cohen (1983) high-dispersion and low-resolution spectrograms (see Zinn & West 1984). Though dated, this metallicity scale is still the most complete (121 GGCs) and homogeneous database available in the literature. In the following, we will label as Z85 the metallicity values listed in column (4) of Table 4 in Armandroff & Zinn (1988) or in column (2) of Table 1 in Zinn (1985).

3.2. *The Carretta & Gratton Scale*

Recently, Carretta & Gratton (1997, hereafter CG97) have presented new measures of chemical abundances using high-dispersion spectra for a set of 24 GGCs, in the metallicity range $-2.24 < [Fe/H]_{Z85} < -0.54$. Though based on a small number of giants (the total sample includes ~ 160 stars, and in many cases only a few giants have been measured in each cluster), these measures have the advantage of measuring *directly* the equivalent widths of Fe I and Fe II lines. Comparing their new abundances with the Z85 metallicities, CG97 concluded that the Z85 scale is not linear and gave a quadratic relation suitable to transform the Z85 scale to their own (see eq. [7] in CG97).

As emphasized by CG97, the transformation relation can be safely used only in the metallicity range $-2.24 < [Fe/H]_{Z85} < -0.54$. In general, the CG97 scale turns out to yield higher metallicity ($\delta[Fe/H] \sim 0.2$) with respect to the Z85 scale for low- to intermediate-metallicity GGCs and lower abundances ($\delta[Fe/H] \sim 0.1$) for metal-rich GGCs.

For the sample of GGCs listed in Table 1 we eventually adopted the metallicity in the CG97 scale ($[Fe/H]_{CG97}$), with the following assumptions:

1. Twenty GGCs have direct spectroscopic measures in CG97. For these clusters the value listed in Table 8 by CG97 has been adopted.
2. Thirty-five GGCs in the quoted range of metallicity ($-2.24 < [Fe/H]_{Z85} < -0.54$) have metallicities only in Z85. For them, we computed $[Fe/H]_{CG97}$ using equation (7) of CG97.
3. Six GGCs in our catalog (namely, NGC 5053, 5927, 6440, 6528, and 6553 and Ter 7) have Z85 values outside the validity range of the transformation to the CG97 scale. For these objects we adopted $[Fe/H]_{CG97} = [Fe/H]_{Z85} + \delta[Fe/H]_{-0.54}$ and $[Fe/H]_{CG97} = [Fe/H]_{Z85} + \delta[Fe/H]_{-2.24}$ for clusters with $[Fe/H]_{Z85} > -0.54$ and $[Fe/H]_{Z85} < -2.24$, respectively, where $\delta[Fe/H]_{-0.54}$ and $\delta[Fe/H]_{-2.24}$ are the corrections, computed via equation (7) of CG97, at $[Fe/H]_{Z85} = -0.54$ and -2.24, respectively.

3.3. *Comparison with Another Recent Catalog*

Rutledge, Hesser, & Stetson (1997, hereafter RHS97) recently used homogeneous observations of the Ca II triplet lines in a sample of 71 GGCs in order to measure an abundance index that should provide a relatively accurate metallicity ranking. They calibrated this index in both the Zinn and CG97 metallicity scales. Figures 1*a* and 1*b* show the residuals between the metallicities by RHS97 (in their Table 2) in the Z85 and CG97 scales, respectively, and the values assumed in this paper for the 42 clusters in common. As can be seen from both panels, most of the clusters lie within ± 0.2 dex (which is a conservative but still reliable level of the global accuracy for metal abundance determinations for GGCs). From Figures 1*a* and 1*b* it is evident that the residuals do not show any trend with respect to the metallicity. Only a few clusters (namely, NGC 5053, NGC 6366, and Ter 7 in Fig. 1*a* and NGC 5053 in Fig. 1*b*), show a larger ($\delta[Fe/H] > 0.4$) scatter and deserve a more accurate spectroscopic analysis.

These considerations strongly suggest that the two sets of measurements are fully consistent within the global assumed uncertainty. In order to use the entire GGC data set we collected, in the following discussion we adopt the metallicity values (in the Zinn and CG97 scales) listed in Table 1. However, for sake of completeness, in § 9 we further discuss the effect of adopting the metallicity measurements listed by RHS97 instead of those listed in Table 1.

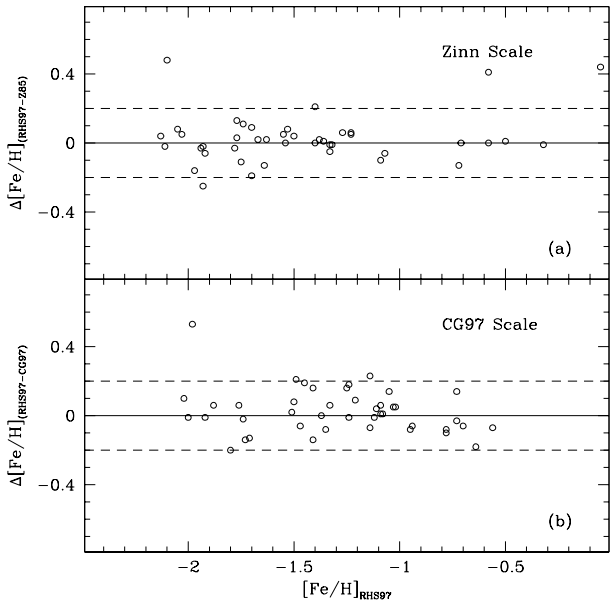

FIG. 1.—Residuals between metallicities from RHS97 (listed in their Table 2), in (*a*) the Zinn and (*b*) the CG97 scale, and the values assumed in this paper (see Table 1) for the 42 clusters in common.

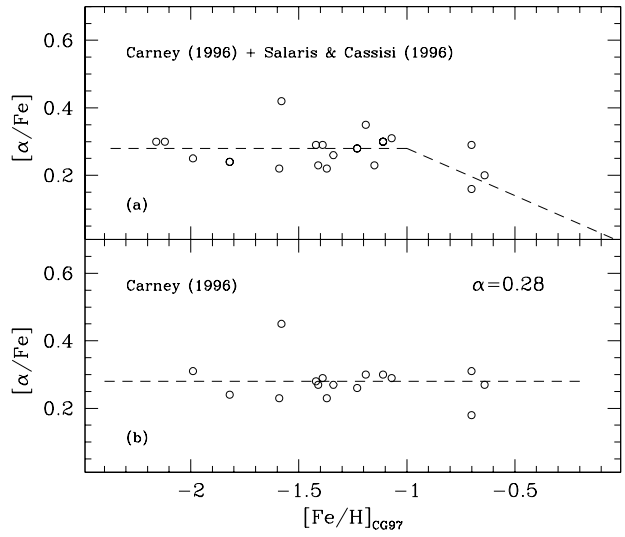

FIG. 2.—Abundance [α/Fe] as a function of $[Fe/H]_{CG97}$. In (*a*), [α/Fe] are from Salaris & Cassisi (1996) and Carney (1996). For the 16 objects in common to the two lists, the [α/Fe] values have been averaged. The dashed line is the enhancement relation as a function of the metallicity that we assumed throughout the paper. In (*b*), [α/Fe] measures are from Carney (1996). The dashed line represents the scenario suggested by Carney (1996) for a constant enhancement with varying metallicity.

3.4. *The Global Metallicity*

In the last decade it has become evident that in Population II stars the abundance of α-elements is enhanced with respect to iron. Direct measurements of the α-elements' abundance in the halo field stars have shown a very well defined behavior as a function of [Fe/H], with a nearly constant overabundance ($[\alpha/Fe] \sim 0.4$) for $[Fe/H] < -2$, and a well-defined trend with metallicity, which linearly decreases to $[\alpha/Fe] \sim 0.0$ as metallicity increases (see Edvardsson et al. 1993; Nissen et al. 1994; Magain 1989; Zhao & Magain 1990; Gratton et al. 1996). In the GGC system the situation is not so clear. The mean overabundance seems to be $[\alpha/Fe] \sim 0.3$, but the behavior with respect to metallicity is still not firmly established. For example, Carney (1996) claims that α-element abundances do not appear to vary as a function of [Fe/H] in GGCs.

There are two recent compilations listing the α-element abundances measured in GGCs: Carney (1996) and Salaris & Cassisi (1996). Especially in the second list the data are collected from different sources and are not the result of independent, self-consistent observations. However, they can be used to have useful quantitative hints.

In our catalog 16 GGCs have values listed in Table 2 of Carney (1996), and 19 in Table 1 of Salaris & Cassisi (1996). There are 16 objects in common in the two lists, and the values are in fairly good agreement (within 0.15 dex). In the following, we will adopt for [α/Fe] the average of the values listed in the two tables. Figure 2*a* shows [α/Fe] as a function of the metallicity in the CG97 scale. Admittedly, it is hard to define a clear-cut trend with metallicity. However, the [α/Fe] abundance for $[Fe/H]_{CG97} < -1$ is compatible with a constant plateau, and for these clusters a mean value of $[\alpha/Fe] = 0.28$ has been adopted. At the metal-rich extreme the situation is less clear. There are only three clusters with $[Fe/H]_{CG97} > -1$. The dashed line in Figure 2*a* shows that their α-element abundances are consistent with a linear decrease with increasing metallicity, similar to that seen in the field stars. For the sake of simplicity, in the following we have thus adopted such a trend for the metal-rich GGCs. However, since the global trend of [α/Fe] with metallicity is still not firmly established, at least for GGCs, especially in the high-metallicity domain, we also considered the scenario suggested by Carney (1996), shown in Figure 2*b*. In this panel only the measures listed by Carney (1996) have been plotted. In § 9, we show what impact the use of the two proposed enhancement relations has on our results.

On the theoretical side, Salaris, Chieffi, & Straniero (1993) have investigated the effect produced on the theoretical evolutionary sequences by considering an enhancement of α-elements. They concluded that α-enhanced isochrones are well mimicked by the standard scaled solar ones, having global metallicity [M/H] given by

$$[M/H] = [Fe/H] + \log (0.638 f_\alpha + 0.362) , \qquad (1)$$

where f_α is the enhancement factor of the α-elements.

Taking into account these prescriptions, we computed the global metallicity listed in column (4) of Table 1 as follows:

1. For the 19 GGCs with [α/Fe] listed by Salaris & Cassisi (1996) or Carney (1996), we adopted $f_\alpha = 10^{[\alpha/Fe]}$.
2. For all the others, we assumed $f_\alpha = 10^{0.28}$ if $[Fe/H] < -0.8$ and $f_\alpha = 10^{-0.35[Fe/H]}$ if $[Fe/H] > -0.8$.

4. MODELING THE RGB AND THE HB: THE STATE OF THE ART

Understanding the observed properties of the H-R diagrams and luminosity functions of GGCs' stars necessarily requires a homogeneous set of H- and He-burning models of low-mass stars and related isochrones. In this paper we have adopted the latest models computed using FRANEC

(Frascati-Raphson-Newton Evolutionary Code), first described by Chieffi & Straniero (1989). The input physics has been recently updated (see, e.g., Straniero, Chieffi, & Limongi 1997, hereafter SCL97). A subset of these models has been presented in SCL97, while the full set will be presented in a forthcoming paper (Chieffi, Limongi, & Straniero 1998a, hereafter CLS98).

The basic assumptions are here briefly summarized:

1. The radiative opacity coefficient is derived from the OPAL tables (Iglesias, Rogers, & Wilson 1992) for temperatures higher then 10^4 K, and from Alexander & Fergusson (1994) at lower temperatures. Thermal conduction is taken from Itoh et al. (1983).

2. The equation of state (EOS) includes quantum relativistic treatment of the electron plasma (electron degeneracy, pair production, and the like). Coulomb corrections are evaluated by means of a Monte Carlo technique using a revised version of the Straniero (1988) EOS in which the partial degeneracy of the electron component is taken into account directly in the Monte Carlo calculations.

3. Thermal neutrino rates due to plasma, photo-, and pair processes are taken into account following the prescription of Munakata, Kohyama, & Itoh (1985), whereas bremsstrahlung and recombination processes are included following Dicus et al. (1976) and Beaudet, Petrosian, & Salpeter (1967), respectively.

4. Nuclear reaction rates are derived from Caughlan & Fowler (1988), except for the $^{12}C(\alpha, \gamma)^{16}O$, for which the rate in Caughlan et al. (1985) is used.

5. The extension of the convective zones is determined by means of the classical Schwarzschild criterion. Induced overshooting and semiconvection during the central He burning is also taken into account (see Castellani et al. 1985). Mixing-length theory is adopted in order to evaluate the temperature gradient in the convective regions. The details of the mixing-length calibrations can be found in SCL97. Breathing pulses occurring at the end of the central He burning phase have been inhibited by adopting the procedure described by Caputo et al. (1989).

6. Microscopic diffusion of He and heavy elements has been included. Note that such a phenomenon mainly affects main-sequence stars, while the properties of post–main-sequence evolution are only slightly changed (see SCL97 for more details).

Thus, models for masses ranging between 0.5 and 1.2 $M_\odot$ have been computed from the zero-age main sequence up to the onset of the He flash. The range of metallicity covers the typical values for GGCs, namely, $0.0001 \leq Z \leq 0.006$. A constant He abundance, $Y = 0.23$, was adopted. Using these models we derived isochrones and luminosity functions for ages ranging between 8 and 20 Gyr.

For the HB, the present set includes models for masses ranging between 0.54 and 0.86 $M_\odot$. The same chemical compositions as in the corresponding H-burning models have been adopted. Following the usual procedure, the core masses and the surface compositions of the ZAHB models are derived from the corresponding last models of the H-burning sequences. Their evolution has been followed from the ZAHB up to central He exhaustion. Few evolutionary sequences have been extended up to the first thermal pulse on the AGB. The procedure adopted to build the ZAHB is fully described by Castellani & Tornambè (1977). Briefly, the first model in our HB sequence has a fully homogeneous H-rich envelope, but the ZAHB model is set when all the secondary elements in the H-burning shell are relaxed to their equilibrium values. This happens when the zero-age model has an age of $\sim 10^6$ yr. Then, the ages of all the subsequent models were rescaled to this zero point.

Finally, all the models have been transposed into the $(V, B-V)$-plane by means of the bolometric corrections and color-temperature relations obtained by Bessell, Castelli, & Plez (1998).

5. THE OBSERVED ZAHB LEVEL: A NEW METHODOLOGICAL APPROACH

Since the first wide series of HB models (Rood 1973), it has been well known that the observed HB cannot be described by any single evolutionary track. It can rather be modeled by convolving a proper set of evolutionary paths of stars having slightly different values of total and/or core mass (Rood 1973). In other words, one can imagine the so-called ZAHB as a sort of starting locus where stars are situated after helium ignition in the core, depending on their total and core mass, and from which they start their evolutionary run toward the AGB. It is thus quite simple (at least in principle) to accurately determine the location of the theoretical ZAHB.

On the observational side, measuring the ZAHB level is unfortunately fairly difficult and sometimes ambiguous. To minimize any possible evolutionary effects off the ZAHB, one might ideally define the ZAHB level by adopting the magnitude of the lower envelope of the observed HB distribution in the region with $0.2 < B-V < 0.6$.

However, the "HB levels" found in the literature are most often not compatible with each other (and not directly comparable), as they actually are the mean level of the HB ($\langle V_{\rm HB} \rangle$), or the mean magnitude of the RR Lyrae stars ($\langle V_{\rm RR} \rangle$), or, finally, the "estimated" ZAHB level. Indeed, the frequent (implicit) assumption that $\langle V_{\rm RR} \rangle$ is coincident with the ZAHB level has been widely criticized (see, e.g., Lee, Demarque, & Zinn 1990), as the actual difference between these two quantities strongly depends on the HB morphology and, in turn, on metallicity (see Carney, Storm, & Jones 1992; Cassisi & Salaris 1997).

To overcome these ambiguities, we have developed a new procedure to redetermine the ZAHB level for all the GGCs listed in our catalog, so as to yield values that could be homogeneous and directly comparable with the corresponding theoretical ones. Using the full set of HB evolutionary tracks described in the previous section, we generated a wide sample of synthetic HBs. The method and the code adopted to derive the synthetic H-R diagrams are described in a forthcoming paper (Chieffi, Straniero, & Limongi 1998b). Briefly, to model an observed HB of a cluster with a given chemical composition, this code requires several input parameters:

$V_{\rm lim}$.—The photometric limiting magnitude of the synthetic CMD.

$N_{\rm HB}$.—The total number of stars with $V < V_{\rm lim}$.

$M_{\rm HB}$.—The mean mass of the HB stars (which drives the position in color of the bulk of the star distribution along the ZAHB).

σ_M.—The width of the Gaussian mass distribution (which drives the spread in color of the HB stars).

Photometric errors.—When comparing the synthetic H-R diagrams with the real ones, we also have to specify the

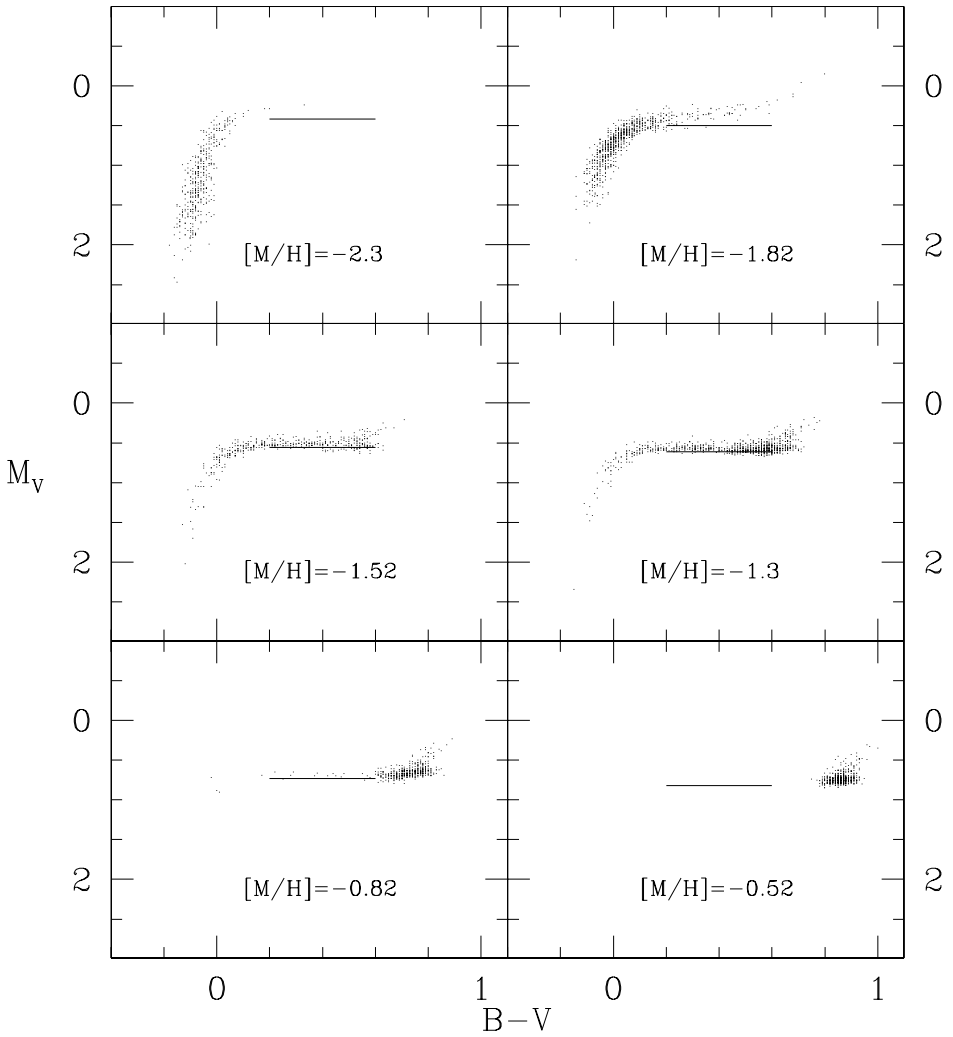

FIG. 3.—Synthetic HBs at different metallicities. The ZAHB level at $\log T_{\rm eff} = 3.85$ is plotted as solid line.

photometric error bar and the completeness of the stellar sample at different luminosity.

By properly tuning these quantities it is possible, in principle, to reproduce any observed HB morphology. For example, σ_M is the main parameter driving the presence and the extension of the HB blue tail. For example, in Figure 3 we show a set of synthetic HBs for six prototype clusters with different metallicity and, in turn, different HB morphologies. The horizontal lines indicate the level of the ZAHB at $\log T_{\rm eff} = 3.85$. As already noted, the lower envelope of the star distribution is not always coincident with the ZAHB level at $\log T_{\rm eff} = 3.85$, and this confirms the need for a careful procedure to yield meaningful and comparable values for the ZAHB.

The problem is illustrated in a more appropriate scale in Figure 4, which shows the evolution of the HB stars off the ZAHB level. From inspection of this figure it is evident that the ZAHB level is not coincident with the lower envelope of the HB star distribution even when the HB is uniformly populated in the RR Lyrae region. This effect is mainly due to the fact that the evolution away from the ZAHB is quite

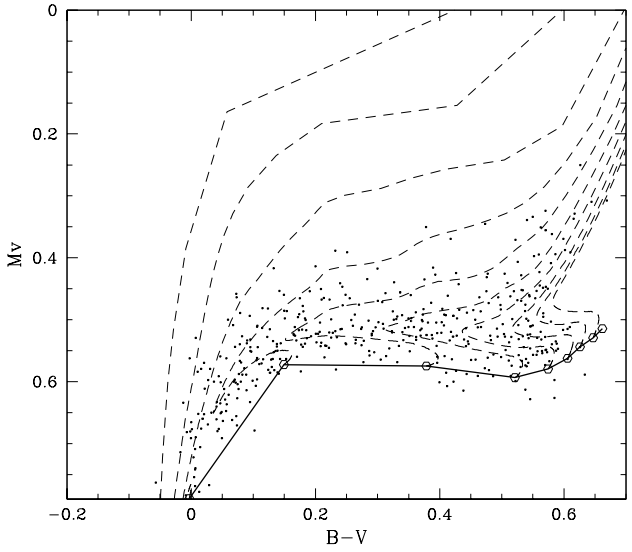

FIG. 4.—Evolutionary tracks for $\log Z = -3.22$ (*dashed lines*) overplotted on a synthetic HB. The heavy solid line is the ZAHB.

TABLE 2

V_{ZAHB}, Metallicities, Reddening, and Derived Distance Moduli for the Program GGCs

Name (1)	$[Fe/H]_{Z85}$ (2)	$[Fe/H]_{CG97}$ (3)	[M/H] (4)	$E(B-V)$ (5)	V_{ZAHB} (6)	$(M-m)_0^{CG97}$ (7)	$(M-m)_0^{[M/H]}$ (8)
NGC 104	−0.71	−0.70	−0.59	0.04	14.22 ± 0.07	13.32	13.29
NGC 288	−1.40	−1.07	−0.85	0.03	15.50 ± 0.10	14.73	14.67
NGC 362	−1.28	−1.15	−0.99	0.05	15.50 ± 0.07	14.68	14.64
NGC 1261.....	−1.31	−1.09	−0.89	0.02	16.72 ± 0.05	15.98	15.93
NGC 1466.....	−1.85	−1.64	−1.44	0.09	19.30 ± 0.07	18.47	18.43
NGC 1841.....	−2.20	−2.11	−1.91	0.18	19.42 ± 0.10	18.39	18.36
NGC 1851.....	−1.29	−1.08	−0.88	0.02	16.20 ± 0.05	15.46	15.41
NGC 1904.....	−1.69	−1.37	−1.22	0.01	16.27 ± 0.07	15.63	15.60
NGC 2419.....	−2.10	−1.97	−1.77	0.03	20.50 ± 0.10	19.92	19.88
NGC 2808.....	−1.37	−1.15	−0.95	0.23	16.27 ± 0.07	14.90	14.85
NGC 3201.....	−1.61	−1.23	−1.03	0.21	14.77 ± 0.07	13.48	13.43
NGC 4147.....	−1.80	−1.58	−1.38	0.02	16.95 ± 0.10	16.32	16.28
NGC 4372.....	−2.08	−1.94	−1.74	0.45	15.90 ± 0.15	14.01	13.97
NGC 4590.....	−2.09	−1.99	−1.81	0.04	15.75 ± 0.05	15.14	15.11
NGC 4833.....	−1.86	−1.58	−1.27	0.33	15.77 ± 0.07	14.18	14.12
NGC 5053.....	−2.58	−2.51	−2.31	0.03	16.70 ± 0.07	16.19	16.17
NGC 5272.....	−1.66	−1.34	−1.16	0.01	15.68 ± 0.05	15.03	14.99
NGC 5286.....	−1.79	−1.57	−1.37	0.24	16.60 ± 0.10	15.29	15.25
NGC 5466.....	−2.22	−2.14	−1.94	0.00	16.62 ± 0.10	16.16	16.12
NGC 5694.....	−1.91	−1.72	−1.52	0.09	18.70 ± 0.10	17.88	17.84
NGC 5824.....	−1.85	−1.64	−1.44	0.14	18.52 ± 0.07	17.53	17.49
NGC 5897.....	−1.68	−1.59	−1.44	0.08	16.45 ± 0.07	15.64	15.61
NGC 5904.....	−1.40	−1.11	−0.90	0.03	15.13 ± 0.05	14.37	14.31
NGC 5927.....	−0.31	−0.46	−0.37	0.47	16.72 ± 0.10	14.41	14.39
NGC 6093.....	−1.64	−1.41	−1.21	0.18	16.12 ± 0.07	14.96	14.92
NGC 6121.....	−1.33	−1.19	−0.94	0.36	13.45 ± 0.10	11.68	11.62
NGC 6171.....	−0.99	−0.87	−0.70	0.33	15.70 ± 0.10	13.95	13.90
NGC 6205.....	−1.65	−1.39	−1.18	0.02	15.10 ± 0.15	14.43	14.38
NGC 6218.....	−1.61	−1.37	−1.17	0.17	14.75 ± 0.15	13.61	13.57
NGC 6229.....	−1.54	−1.30	−1.10	0.01	18.11 ± 0.05	17.45	17.41
NGC 6254.....	−1.60	−1.41	−1.25	0.28	14.85 ± 0.10	13.38	13.35
NGC 6266.....	−1.28	−1.07	−0.87	0.47	16.40 ± 0.20	14.26	14.21
NGC 6333.....	−1.78	−1.56	−1.36	0.36	16.35 ± 0.15	14.67	14.62
NGC 6341.....	−2.24	−2.16	−1.95	0.02	15.30 ± 0.10	14.78	14.74
NGC 6352.....	−0.51	−0.64	−0.50	0.21	15.30 ± 0.10	13.85	13.81
NGC 6366.....	−0.99	−0.87	−0.70	0.69	15.80 ± 0.10	12.93	12.88
NGC 6397.....	−1.91	−1.82	−1.65	0.18	13.00 ± 0.10	11.92	11.89
NGC 6440.....	−0.34	−0.49	−0.40	1.09	18.70 ± 0.20	14.48	14.45
NGC 6528.....	−0.23	−0.38	−0.31	0.62	17.17 ± 0.20	14.37	14.35
NGC 6535.....	−1.75	−1.53	−1.33	0.32	15.90 ± 0.15	14.33	14.29
NGC 6553.....	−0.29	−0.44	−0.36	0.84	16.92 ± 0.20	13.46	13.44
NGC 6584.....	−1.54	−1.30	−1.10	0.11	16.60 ± 0.05	15.63	15.59
NGC 6637.....	−0.59	−0.68	−0.55	0.17	15.95 ± 0.10	14.64	14.60
NGC 6652.....	−0.99	−0.87	−0.70	0.09	16.07 ± 0.10	15.06	15.01
NGC 6681.....	−1.51	−1.27	−1.07	0.07	15.85 ± 0.10	15.00	14.95
NGC 6712.....	−1.01	−0.88	−0.71	0.46	16.32 ± 0.07	14.16	14.12
NGC 6717.....	−1.32	−1.10	−0.90	0.21	15.75 ± 0.15	14.43	14.38
NGC 6752.....	−1.54	−1.42	−1.21	0.04	13.90 ± 0.15	13.18	13.13
NGC 6809.....	−1.82	−1.61	−1.41	0.07	14.60 ± 0.10	13.82	13.78
NGC 6838.....	−0.58	−0.70	−0.49	0.25	14.52 ± 0.10	12.97	12.90
NGC 6934.....	−1.54	−1.30	−1.10	0.11	16.97 ± 0.07	16.00	15.96
NGC 6981.....	−1.54	−1.30	−1.10	0.05	16.86 ± 0.07	16.08	16.03
NGC 7006.....	−1.59	−1.35	−1.15	0.05	18.85 ± 0.15	18.08	18.03
NGC 7078.....	−2.17	−2.12	−1.91	0.09	15.90 ± 0.07	15.15	15.12
NGC 7099.....	−2.13	−1.91	−1.71	0.03	15.30 ± 0.10	14.71	14.67
NGC 7492.....	−1.51	−1.27	−1.07	0.00	17.78 ± 0.10	17.15	17.10
IC 4499	−1.50	−1.26	−1.06	0.24	17.70 ± 0.07	16.32	16.27
Rup 106	−1.90	−1.70	−1.50	0.21	17.85 ± 0.10	16.66	16.62
Arp 2.....	−1.85	−1.64	−1.44	0.11	18.30 ± 0.15	17.41	17.37
Ter 7	−0.49	−0.64	−0.52	0.06	17.87 ± 0.10	16.89	16.85
Ter 8	−1.81	−1.60	−1.40	0.14	18.15 ± 0.10	17.16	17.11

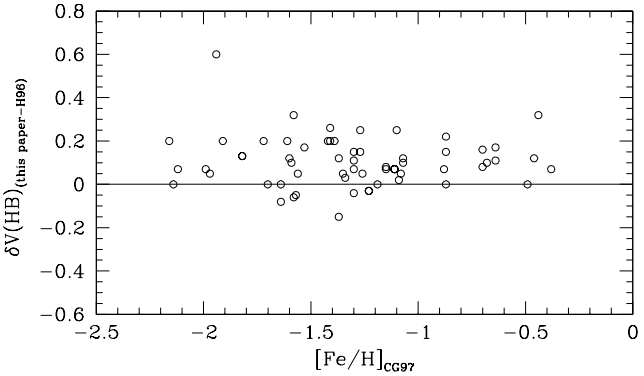

FIG. 5.—Differences between the V_{ZAHB} level obtained in this paper and the V_{HB} listed by H96.

rapid at the beginning. After only 8 Myr ($\sim$8% of the total lifetime on the HB), the stars are already 0.05–0.1 mag brighter than the ZAHB *starting line*, then they spend $\sim$70% of the total HB time in covering the next 0.1 mag. Thus the near-ZAHB HB is inherently poorly populated, and the observed lower envelope of the HB will be a poor measure of the "HB level" that is affected both by the sample size and the size of the photometric errors.

To overcome the problem we have adopted the following empirical procedure:

1. For each cluster in our catalog we computed a synthetic HB (with the appropriate abundances), tuning the parameters so as to best reproduce the observed HB morphology.
2. The synthetic HB was shifted in magnitude and color to match the observed HB.
3. The "observed" V_{ZAHB} value is then read from the line indicating the theoretical ZAHB level at $\log T_{eff} = 3.85$ as yielded by the best-fitting synthetic HB.

Note that this procedure makes use of the models only as a guide to drawing of the location of the "true" ZAHB level and is only slightly dependent on the adopted theoretical models. It avoids the uncertainties induced by the differences in the observed HB morphologies and yields values obtained with a homogeneous and self-consistent empirical method. ZAHB levels determined in this way should be especially appropriate to compare with theoretical models. The V_{ZAHB} values thus obtained are listed in column (6) of Table 2. The errors in V_{ZAHB} have been estimated by combining the scatter from multiple independent determinations of the ZAHB level and an estimate of the photometric error (at the HB level) in each cluster.

Although the actual difference between V_{ZAHB} and $\langle V_{HB}\rangle$ depends on the various parameters (such as the mean star mass, the core mass, the metallicity, helium abundance) that drive the HB morphology, on the basis of the synthetic HB plotted in Figures 3 and 4 we derived the following average relation:

$$V_{ZAHB} = \langle V_{HB}\rangle + 0.106[M/H]^2 + 0.236[M/H] + 0.193 , \quad (2)$$

which can be used, to first order, to derive the V_{ZAHB} level from the $\langle V_{HB}\rangle$ measured in the color range $0.2 < B-V < 0.6$. Note that for metal-rich clusters ([M/H] > -1), the mean value of the red HB clump was assumed to be $\langle V_{HB}\rangle$. The relation suggests that the minimum difference between ZAHB and mean HB luminosity ($\delta V \sim 0.06$) occurs at [M/H] ~ -1.2, and it turns out to be $\delta V \sim 0.16$ and $\sim$0.10 at [M/H] $= -2.2$ and -0.5, respectively.

We can compare the adopted V_{ZAHB} values listed in Table 2, for instance, with those listed in the recent compilation by Harris (1996, hereafter H96). The residuals (this paper minus H96) are plotted versus $[Fe/H]_{CG97}$ in Figure 5. As expected, there is a clear systematic difference ($\sim$0.17 mag) between the two, with the values derived in this paper being fainter than those listed by H96. Only one cluster (NGC 4372) shows a large ($\delta V > 0.4$) residual. This is because of the fact that H96 adopted different (older) photometry (with a different photometric zero point) than that used in this paper. Similar comparisons can be made with other compilations, such as Buonanno, Corsi, & Fusi Pecci (1989, hereafter BCF89) and Chaboyer, Demarque, & Sarajedini (1996). In both cases the V_{HB} values listed in Table 2 are systematically fainter ($\delta V \sim 0.1$ and $\delta V \sim 0.15$, respectively).

6. THE RED GIANT BRANCH

6.1. *The RGB Mean Ridgeline*

In order to derive the mean ridgeline of the RGB for all the GGCs listed in our catalog, we adopted the following procedure:

1. A rough preliminary selection of the stars belonging to the RGB (excluding the HB and AGB stars) was performed by eye to initialize and to accelerate the subsequent iterations.
2. The polynomial fitting technique presented by Sarajedini & Norris (1994, hereafter SN94) was then applied to the samples. In particular, the RGB has been fitted by a (second- or third-order) polynomial law of the form $B-V = f(V)$. After each iteration, stars more than 2 σ in color from the best-fitting ridgeline were rejected and the fitting procedure repeated to yield a stable solution.

6.2. *Photometric Parameters along the RGB*

As is widely known, RGB morphology and location in the CMD are good metallicity indicators of the parent cluster. In particular, three main parameters have been defined to describe the photometric characteristics of the RGB:

ΔV.—First defined by Sandage & Wallerstein (1960), as a measure of the height of the RGB brighter than the HB level. They used $\Delta V_{1.4}$ (in mag), with V_{RGB} measured at the intrinsic color $(B-V)_0 = 1.4$. Recently, Sarajedini & Layden (1997, hereafter SL97) have defined two similar parameters, $\Delta V_{1.1}$ and $\Delta V_{1.2}$, measured at $(B-V)_0 = 1.1$ and $(B-V)_0 = 1.2$, respectively. These two additional parameters are particularly useful since the observed samples are often not populated enough at $(B-V)_0 = 1.4$ to clearly define a mean ridgeline.

$(B-V)_{0,g}$.—Defined by Sandage & Smith (1966) as the intrinsic color of the RGB at the HB level.

S.—Defined by Hartwick (1968) (and here called $S_{2.5}$) as the slope of the line connecting two points along the RGB, the first being the intersection of the RGB with the line defining the HB level and the second being the point on the RGB 2.5 mag brighter than the HB. Following SL97, we

have also defined $S_{2.0}$, which is based on the RGB point only 2.0 mag brighter than the HB level.

Over the past 15 years, many calibrations of these parameters in terms of metallicity have been proposed (see Table 5 in Ferraro et al. 1992b and, more recently, SL97, Carretta & Bragaglia 1998, and Table 7 in Borissova et al. 1999). We present here revised calibrations making use of the wider and more homogeneous data set now available. The six parameters defined above [namely, $\Delta V_{1.1}$, $\Delta V_{1.2}$, $\Delta V_{1.4}$, $(B-V)_{0,g}$, $S_{2.0}$, and $S_{2.5}$] have been measured for all the GGCs listed in our catalog that have suitable data in the $(V, B-V)$-plane. No attempt has been made to extrapolate the mean ridgeline beyond the sufficiently populated regions of the available CMDs. The values measured are listed in Table 3. The main source of uncertainty in these measures is the propagation of the error in the determination of the ZAHB level. Thus, the uncertainty on the $V_{\rm ZAHB}$ ($\sim$0.10) typically produces a comparable uncertainty ($\delta \sim 0.1$ mag) in measuring ΔV-parameters, an error $\delta \sim 0.03$ mag in the determination of the color $(B-V)_{0,g}$, and a significantly larger error ($\delta \sim 0.2$–0.3) in deriving the S-parameters.

In Figures 6–11, the RGB observables are plotted versus the metal abundances $[{\rm Fe/H}]_{\rm CG97}$ (Figs. 6*a*–11*a*) and the global metallicities [M/H] (Figs. 6*b*–11*b*). The solid lines overplotted in each figure are the best fits to the data, given in analytic form in Table 4. In deriving these relations, the 20 GGCs with direct spectroscopic measures of [Fe/H] and direct measures of the [α/Fe] abundance (excepting NGC 7099) have been considered as primary calibrators and have been assigned higher weights in determining the best-fit relations. These primary calibrators are plotted as filled circles. Two clusters (NGC 5053 and NGC 5694), which have the largest deviations in Figure 10 (*dotted circles*), have been excluded during the fitting procedure. In both excluded clusters, the observed samples of the upper RGB are so poorly populated that the location of the branch at that level is quite uncertain. NGC 5053 has been excluded, for the same reason, in deriving the calibration of the parameter $S_{2.0}$ (see Fig. 11). The relationships of all the RGB parameters defined above in terms of the spectroscopic and *global* metallicity scales are reported in Table 4. Note that the quoted relations can be safely used only in the metallicity range covered by the adopted sample (i.e., roughly $-2.5 < [{\rm Fe/H}]_{\rm CG97} < -0.5$ and $-2.3 < [{\rm M/H}] < -0.4$). This range should be considered as a first guess, and the reader is requested to refer to each figure (Figs. 6–11) to check the exact range of metallicity within which each relation has been derived.

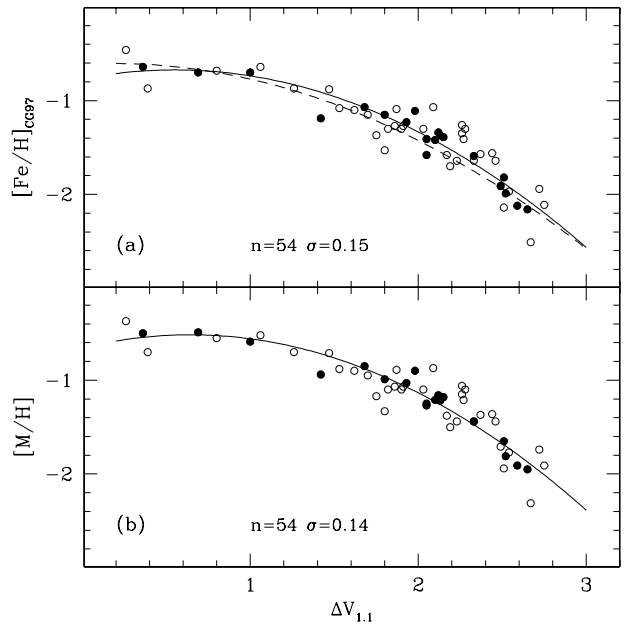

FIG. 6.—Calibration of the parameter $\Delta V_{1.1}$ with respect to (*a*) $[{\rm Fe/H}]_{\rm CG97}$ and (*b*) the global metallicity ([M/H]). The filled circles represent clusters for which spectroscopic metallicity and [α/Fe] abundance has been directly measured. The solid lines are the best fit to the data. The dashed line in (*a*) is the relation recently obtained by Carretta & Bragaglia (1998). The number of clusters used to compute each relation is reported together with the standard deviations of the data.

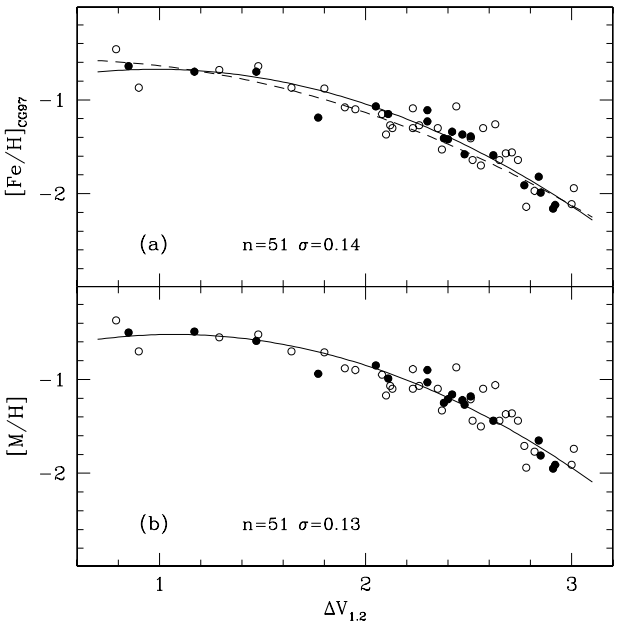

FIG. 7.—Same as Fig. 6, but for the parameter $\Delta V_{1.2}$

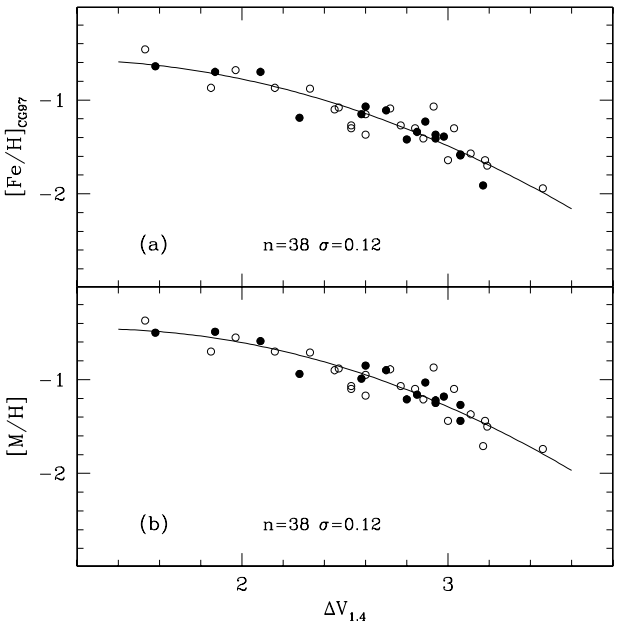

FIG. 8.—Same as Fig. 6, but for the parameter $\Delta V_{1.4}$

TABLE 3

RGB Parameters

Name	$[Fe/H]_{CG97}$	[M/H]	$\Delta V_{1.1}$	$\Delta V_{1.2}$	$\Delta V_{1.4}$	$(B-V)_{0,g}$	$S_{2.5}$	$S_{2.0}$	$(B-V)_{0,-1}$
NGC 104	−0.70	−0.59	1.00	1.47	2.09	0.95	...	4.82	1.29
NGC 288	−1.07	−0.85	1.68	2.05	2.60	0.83	4.71	5.59	1.12
NGC 362	−1.15	−0.99	1.80	2.11	2.58	0.81	4.50	5.59	1.07
NGC 1261.....	−1.09	−0.89	1.87	2.23	2.72	0.83	5.27	6.54	1.07
NGC 1466.....	−1.64	−1.44	2.23	2.52	3.00	0.73	5.37	6.54	0.93
NGC 1841.....	−2.11	−1.91	2.75	3.00	...	0.63	6.53	7.90	0.80
NGC 1851.....	−1.08	−0.88	1.53	1.90	2.47	0.86	4.52	5.41	1.15
NGC 1904.....	−1.37	−1.22	2.13	2.47	2.94	0.78	5.86	7.01	1.00
NGC 2419.....	−1.97	−1.77	2.54	2.82	...	0.72	6.78	8.37	0.88
NGC 2808.....	−1.15	−0.95	1.70	2.08	2.60	0.85	4.92	6.06	1.10
NGC 3201.....	−1.23	−1.03	1.93	2.30	2.89	0.79	5.34	6.14	1.05
NGC 4147.....	−1.58	−1.38	2.17	...	...	0.76	...	6.63	0.99
NGC 4372.....	−1.94	−1.74	2.72	3.01	3.46	0.68	7.05	8.49	0.83
NGC 4590.....	−1.99	−1.81	2.52	2.85	...	0.71	6.54	7.65	0.88
NGC 4833.....	−1.58	−1.27	2.05	2.48	3.06	0.81	6.38	7.26	1.01
NGC 5053.....	−2.51	−2.31	2.67	...	...	0.67	6.46	7.31	0.84
NGC 5272.....	−1.34	−1.16	2.12	2.42	2.85	0.78	5.58	6.98	0.99
NGC 5286.....	−1.57	−1.37	2.37	2.68	3.11	0.72	5.98	6.99	0.93
NGC 5466.....	−2.14	−1.94	2.51	2.78	...	0.74	7.06	9.44	0.86
NGC 5694.....	−1.72	−1.52	...	...	...	0.70	7.46	8.29	0.87
NGC 5824.....	−1.64	−1.44	2.46	2.74	3.18	0.70	6.11	7.39	0.89
NGC 5897.....	−1.59	−1.44	2.33	2.62	3.06	0.75	6.07	7.55	0.93
NGC 5904.....	−1.11	−0.90	1.98	2.30	2.70	0.81	5.20	6.66	1.04
NGC 5927.....	−0.46	−0.37	0.26	0.79	1.53	1.06	...	3.96	1.52
NGC 6093.....	−1.41	−1.21	2.27	2.51	2.88	0.70	5.02	6.37	0.92
NGC 6121.....	−1.19	−0.94	1.42	1.77	2.28	0.90	4.06	5.18	1.18
NGC 6171.....	−0.87	−0.70	1.26	1.64	2.16	0.92	3.76	4.92	1.24
NGC 6205.....	−1.39	−1.18	2.15	2.51	2.98	0.76	5.78	6.73	0.98
NGC 6218.....	−1.37	−1.17	1.75	2.10	2.60	0.85	4.95	6.22	1.08
NGC 6229.....	−1.30	−1.10	1.82	2.13	2.53	0.85	4.75	6.63	1.07
NGC 6254.....	−1.41	−1.25	2.05	2.38	2.94	0.74	5.00	5.74	1.00
NGC 6266.....	−1.07	−0.87	2.09	2.44	2.93	0.77	5.55	6.48	1.02
NGC 6333.....	−1.56	−1.36	2.44	2.71	...	0.79	...	...	0.92
NGC 6341.....	−2.16	−1.95	2.65	2.91	...	0.71	7.39	9.74	0.83
NGC 6352.....	−0.64	−0.50	0.36	0.85	1.58	1.04	...	3.99	1.49
NGC 6366.....	−0.87	−0.70	0.39	0.90	1.85	1.03	...	4.79	1.38
NGC 6397.....	−1.82	−1.65	2.51	2.84	...	0.71	6.42	7.51	0.89
NGC 6440.....	−0.49	−0.40	...	...	...	...	...	...	...
NGC 6528.....	−0.38	−0.31	...	...	...	...	...	...	...
NGC 6535.....	−1.53	−1.33	1.80	2.37	...	0.86	...	7.31	1.07
NGC 6553.....	−0.44	−0.36	...	...	...	...	...	...	...
NGC 6584.....	−1.30	−1.10	2.03	2.35	2.84	0.77	5.17	6.24	1.01
NGC 6637.....	−0.68	−0.55	0.80	1.29	1.97	0.98	3.89	4.65	1.35
NGC 6652.....	−0.87	−0.70	...	...	...	...	...	...	...
NGC 6681.....	−1.27	−1.07	1.91	2.26	2.77	0.80	5.20	6.27	1.05
NGC 6712.....	−0.88	−0.71	1.47	1.80	2.33	0.85	4.00	4.81	1.19
NGC 6717.....	−1.10	−0.90	1.62	1.95	2.45	0.83	4.19	5.14	1.13
NGC 6752.....	−1.42	−1.21	2.10	2.40	2.80	0.80	5.67	7.25	1.00
NGC 6809.....	−1.61	−1.41	...	...	...	...	...	...	...
NGC 6838.....	−0.70	−0.49	0.69	1.17	1.87	1.00	3.91	4.44	1.39
NGC 6934.....	−1.30	−1.10	2.28	2.57	3.03	0.73	5.69	6.94	0.95
NGC 6981.....	−1.30	−1.10	1.90	2.23	...	0.81	5.05	6.26	1.04
NGC 7006.....	−1.35	−1.15	2.26	...	...	0.76	6.36	7.10	0.98
NGC 7078.....	−2.12	−1.91	2.59	2.92	...	0.69	6.53	7.62	0.86
NGC 7099.....	−1.91	−1.71	2.49	2.77	3.17	0.73	6.63	8.08	0.89
NGC 7492.....	−1.27	−1.07	1.86	2.12	2.53	0.76	4.00	5.05	1.04
IC 4499	−1.26	−1.06	2.26	2.63	...	0.74	5.95	6.75	0.97
Rup 106	−1.70	−1.50	2.19	2.56	3.19	0.73	5.55	6.20	0.96
Arp 2.....	−1.64	−1.44	2.33	2.65	...	0.73	5.97	7.17	0.92
Ter 7	−0.64	−0.52	1.06	1.48	...	0.94	...	...	1.30
Ter 8	−1.60	−1.40	...	...	...	...	...	...	...

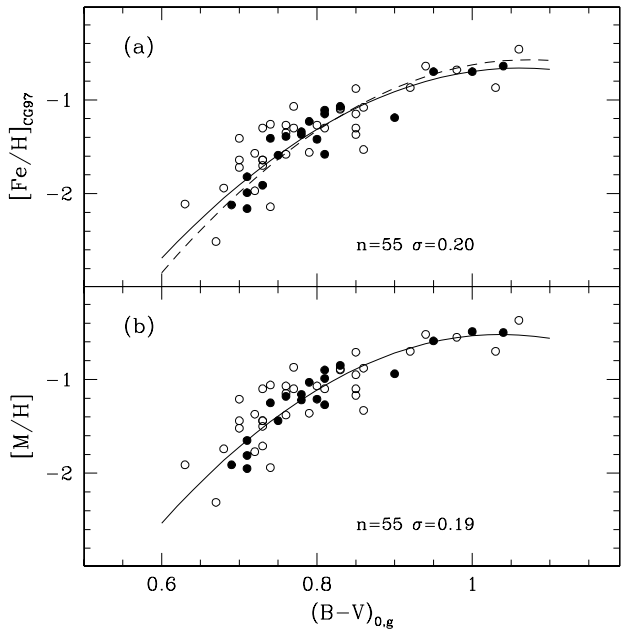

FIG. 9.—Same as Fig. 6, but for the parameter $(B-V)_{0,g}$

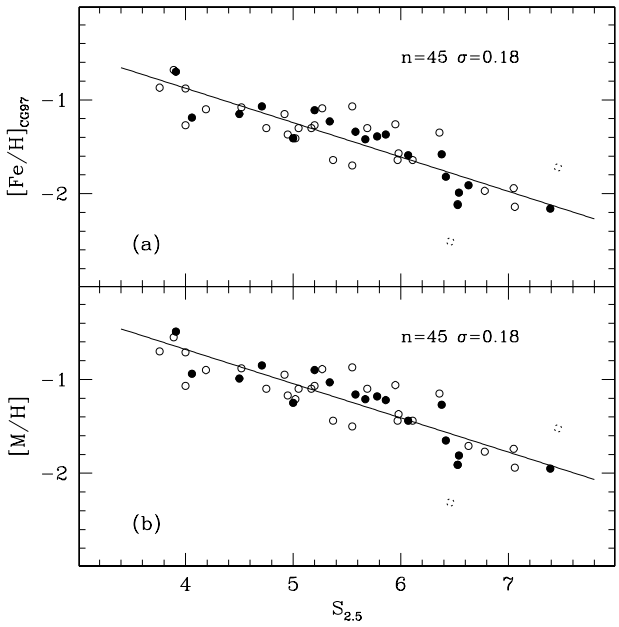

FIG. 10.—Same as Fig. 6, but for the parameter $S_{2.5}$. Two clusters (NGC 5053 and NGC 5694; *dotted circles*) have been excluded from the determination of the fitting relation (see text).

Similar relations for $\Delta V_{1.1}$, $\Delta V_{1.2}$ and $(B-V)_{0,g}$ have been obtained recently by Carretta & Bragaglia (1998), who used the values listed by SL97 and SN94. For the sake of comparison, their relations have been plotted as dashed lines in the corresponding figures. The differences can easily be understood as being due to the combination of two main factors:

1. Different assumptions about the HB level. There are differences of up to 0.15 mag between the HB levels adopted here and those listed in SL97 and SN94. These differences directly affect the measure of the ΔV-parameters, and this explains most of the offset between the solid and the dashed lines in Figures 5*a* and 6*a*.

2. The small sample (only nine GGCs) considered by Carretta & Bragaglia (1998). This mainly affects the fit at the extremes. In fact, the dashed lines significantly deviate from the solid line at the extremes of the metallicity scale (see Figs. 6*a*, 7*a*, 9*a*).

6.3. *The SRM in the* $(V, B-V)$*-Plane*

The equations reported in Table 4 represent a system that can be used to *simultaneously* derive very useful estimates of metal abundance ($[Fe/H]_{CG97}$ and [M/H]) and reddening from the morphology and location of the RGB (the so-

TABLE 4

RGB PARAMETERS AND THEIR CALIBRATION IN TERMS OF DIFFERENT METALLICITY SCALES

No.	Relation	Fit
	Relations in Terms of $[Fe/H]_{CG97}$	
(4.1)	$[Fe/H]_{CG97} = -0.315\Delta V_{1.1}^2 + 0.347\Delta V_{1.1} - 0.768$	$n = 54$, $\sigma = 0.15$
(4.2)	$[Fe/H]_{CG97} = -0.359\Delta V_{1.2}^2 + 0.708\Delta V_{1.2} - 1.023$	$n = 51$, $\sigma = 0.14$
(4.3)	$[Fe/H]_{CG97} = -0.252\Delta V_{1.4}^2 + 0.548\Delta V_{1.4} - 0.864$	$n = 38$, $\sigma = 0.12$
(4.4)	$[Fe/H]_{CG97} = -9.47(B-V)_{0,g}^2 + 20.127(B-V)_{0,g} - 11.36$	$n = 55$, $\sigma = 0.20$
(4.5)	$[Fe/H]_{CG97} = -0.37S_{2.5} + 0.59$	$n = 45$, $\sigma = 0.18$
(4.6)	$[Fe/H]_{CG97} = -0.28S_{2.0} + 0.67$	$n = 52$, $\sigma = 0.18$
(4.7)	$(B-V)_{0,g} = 0.005[Fe/H]_{CG97}^3 + 0.118[Fe/H]_{CG97}^2 + 0.489[Fe/H]_{CG97} + 1.243$	$n = 55$, $\sigma = 0.04$
	Relations in Terms of [M/H]	
(4.8)	$[M/H] = -0.337\Delta V_{1.1}^2 + 0.434\Delta V_{1.1} - 0.656$	$n = 54$, $\sigma = 0.14$
(4.9)	$[M/H] = -0.382\Delta V_{1.2}^2 + 0.820\Delta V_{1.2} - 0.960$	$n = 51$, $\sigma = 0.13$
(4.10).....	$[M/H] = -0.280\Delta V_{1.4}^2 + 0.717\Delta V_{1.4} - 0.918$	$n = 38$, $\sigma = 0.12$
(4.11).....	$[M/H] = -10.513(B-V)_{0,g}^2 + 21.813(B-V)_{0,g} - 11.835$	$n = 55$, $\sigma = 0.19$
(4.12).....	$[M/H] = -0.36S_{2.5} + 0.78$	$n = 45$, $\sigma = 0.18$
(4.13).....	$[M/H] = -0.29S_{2.0} + 0.53$	$n = 52$, $\sigma = 0.18$
(4.14).....	$(B-V)_{0,g} = 0.04[M/H]^3 + 0.275[M/H]^2 + 0.67[M/H] + 1.252$	$n = 55$, $\sigma = 0.04$
	The Parameter $(B-V)_{0,-1}$ vs. Metallicity	
(4.15).....	$(B-V)_{0,-1} = 0.055[Fe/H]_{CG97}^3 + 0.448[Fe/H]_{CG97}^2 + 1.255[Fe/H]_{CG97} + 2.023$	$n = 55$, $\sigma = 0.05$
(4.16).....	$(B-V)_{0,-1} = 0.115[M/H]^3 + 0.695[M/H]^2 + 1.496[M/H] + 1.983$	$n = 55$, $\sigma = 0.05$

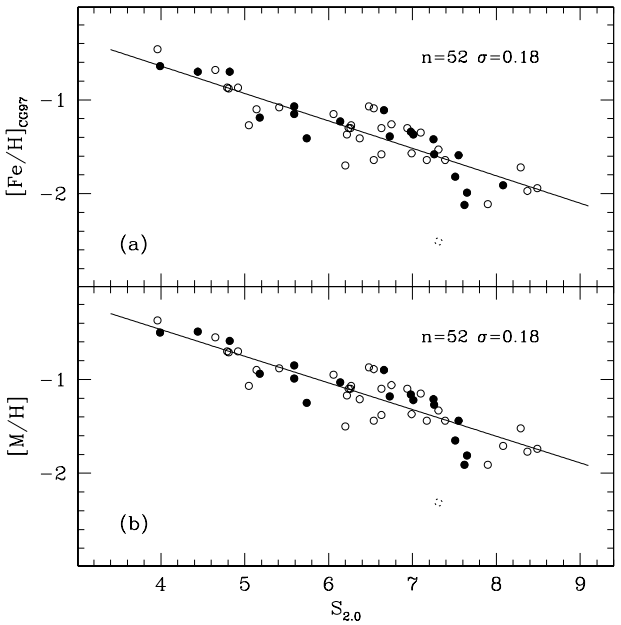

FIG. 11.—Same as Fig. 6, but for the parameter $S_{2.0}$

called SRM method; Sarajedini 1994b). By using the system of equations in Table 4, one can choose the most appropriate observables (measurable in the CMD depending on the actual extension of the observed RGB) and then proceed as follows:

1. Since parameters $S_{2.0}$ and $S_{2.5}$ are independent of cluster reddening, from equations (4.5) and (4.6) it is possible to obtain a first guess for the cluster metallicity, $[\mathrm{Fe/H}]_i$, and similarly for $[\mathrm{M/H}]_i$ using equations (4.12) and (4.13).

2. Introducing then $[\mathrm{Fe/H}]_i$ in equation (4.7), it is possible to derive a first value for the expected $(B-V)_{0,g}$ and, in turn, a first estimate for the reddening from $E(B-V) = (B-V)_g - (B-V)_{0,g}$.

3. Using this first estimate of the reddening it is then possible to derive $\Delta V_{1.1}$, $\Delta V_{1.2}$, and $\Delta V_{1.4}$ and, from equations (4.1), (4.2), and (4.3), a new determination of the metallicity.

4. By iterating the procedure one can quickly achieve convergence, yielding values for reddening and the metallicities generally accurate to about $\delta[\mathrm{Fe/H}] < 0.1$ and $\delta E(B-V) < 0.02$.

6.4. *The RGB Bump: The New Database*

One of the most intriguing features along the RGB is the so-called RGB bump, the existence of which had been predicted since the early theoretical models (Thomas 1967; Iben 1968) but which was only first observed years later (King, Da Costa, & Demarque 1985), as the observed samples were not populous enough to allow a firm detection. In fact, a very large sample of stars, with more than 1000 in the upper 4 mag of the RGB, is necessary to safely distinguish this feature from statistical fluctuations. This problem is more severe for metal-poor clusters, as a consequence of the dependence of the luminosity of the bump on metallicity: the luminosity increases with decreasing metallicity. So, in metal-poor GGCs the bump is shifted toward the RGB tip, in a region that is intrinsically poorly populated, and where the detection is difficult even when large samples are available.

The first systematic study of the location of the RGB bump in GGCs was presented by F90, who reported the identification of the bump in a sample of 11 GGCs. They presented a detailed comparison with theoretical models (Rood & Crocker 1989; R. T. Rood 1987, unpublished) based on old input physics. This first comparison showed that while the dependence of bump luminosity on metallicity was nicely reproduced by theoretical models, there was a substantial disagreement in the zero point, the theoretical relation being about 0.4 mag brighter than the observations. Alongi et al. (1991) interpreted this disagreement as evidence of the limit of the standard models in describing the correct location of the RGB bump. Thus, in order to reconcile observations and theory, they claimed the occurrence of an additional mixing process below the bottom of the convective envelope of an RGB star (i.e., *undershooting*). Straniero, Chieffi, & Salaris (1992) and Ferraro (1992), however, independently pointed out that proper inclusion of the α-element enhancement in the computation of the global metallicity of the parent cluster could reduce the discrepancy. In a recent review of the problem, Cassisi & Salaris (1997) essentially reobtained the same result.

Since the early work presented in F90, the RGB bump has been identified in a growing number of GGCs (see, e.g., Brocato et al. 1996). As pointed out by Rood & Crocker (1985), the best tool to identify the RGB bump is the luminosity function (LF), and both the integrated and the differential LFs are useful (Ferraro 1992). Following the prescriptions of F90, we independently identified the RGB bump in 47 GGCs in our catalog. The bump magnitudes so measured are listed in column (5) of Table 5. This represents the largest GGCs sample listing the RGB bump locations available so far.

To allow comparisons with both previous studies and theoretical models, following F90, we have measured the parameter $\Delta V_{\mathrm{HB}}^{\mathrm{bump}} = V_{\mathrm{bump}} - V_{\mathrm{HB}}$, which has the advantage of actually being independent of the photometric zero point of the cluster data, the reddening, and the distance modulus (DM). Moreover, we have also adopted the parameter s, defined as $s = \sinh^{-1}(Z/0.00025)$, where $Z = 10^{[\mathrm{Fe/H}]-1.7}$. This quantity is best suited to linearly describe the dependence of $\Delta V_{\mathrm{HB}}^{\mathrm{bump}}$ on metallicity (F90).

As a starting point, we first adopt the same metallicity scale as F90, namely, the Zinn (1985) scale. In Figure 12*a*, we report $\Delta V_{\mathrm{HB}}^{\mathrm{bump}}$ as a function of [Fe/H], while in Figure 12*b* the same quantity is plotted versus s. As can be seen, there is a clear-cut correlation. The error bars, as expected, tend to be systematically larger at lower metallicities, as a result of the difficulty, mentioned above, in identifying the bump in those GGCs.

The best fit to the data obtained by F90 is also overplotted on the new values in the same figure. As can be seen there is a systematic shift, the new values being slightly lower than the old ones, by about 0.05–0.1 mag. Such a difference is mainly due to the new procedure used to measure the ZAHB level. In fact, in F90 the lower edges of the observed HB distributions were assumed to be coincident with the ZAHB levels (see the discussion presented in § 4).

On the theoretical side, the latest models that include improvements in the input physics imply a reduction of the

TABLE 5

RGB AND AGB BUMP PARAMETERS

Name (1)	$[Fe/H]_{CG97}$ (2)	[M/H] (3)	V_{ZAHB} (4)	V_{RGB}^{bump} (5)	V_{AGB}^{bump} (6)
NGC 104	−0.70	−0.59	14.22 ± 0.07	14.55 ± 0.05	13.15 ± 0.07
NGC 288	−1.07	−0.85	15.50 ± 0.10	15.45 ± 0.05	...
NGC 362	−1.15	−0.99	15.50 ± 0.07	15.40 ± 0.10	...
NGC 1261.....	−1.09	−0.89	16.72 ± 0.05	16.60 ± 0.05	15.65 ± 0.05
NGC 1466.....	−1.64	−1.44	19.30 ± 0.07	...	...
NGC 1841.....	−2.11	−1.91	19.42 ± 0.10	...	18.55 ± 0.10
NGC 1851.....	−1.08	−0.88	16.20 ± 0.05	16.15 ± 0.05	...
NGC 1904.....	−1.37	−1.22	16.27 ± 0.07	15.95 ± 0.05	...
NGC 2419.....	−1.97	−1.77	20.50 ± 0.10	...	...
NGC 2808.....	−1.15	−0.95	16.27 ± 0.07	16.15 ± 0.05	15.20 ± 0.07
NGC 3201.....	−1.23	−1.03	14.77 ± 0.07	14.55 ± 0.05	...
NGC 4147.....	−1.58	−1.38	16.95 ± 0.10	...	...
NGC 4372.....	−1.94	−1.74	15.90 ± 0.15	...	...
NGC 4590.....	−1.99	−1.81	15.75 ± 0.05	15.15 ± 0.05	...
NGC 4833.....	−1.58	−1.27	15.77 ± 0.07	15.35 ± 0.05	...
NGC 5053.....	−2.51	−2.31	16.70 ± 0.07	...	...
NGC 5272.....	−1.34	−1.16	15.68 ± 0.05	15.45 ± 0.05	14.80 ± 0.05
NGC 5286.....	−1.57	−1.37	16.60 ± 0.10	16.25 ± 0.05	15.57 ± 0.10
NGC 5466.....	−2.14	−1.94	16.62 ± 0.10	...	...
NGC 5694.....	−1.72	−1.52	18.70 ± 0.10	18.15 ± 0.07	...
NGC 5824.....	−1.64	−1.44	18.52 ± 0.07	...	...
NGC 5897.....	−1.59	−1.44	16.45 ± 0.07	16.00 ± 0.10	...
NGC 5904.....	−1.11	−0.90	15.13 ± 0.05	15.00 ± 0.05	14.15 ± 0.05
NGC 5927.....	−0.46	−0.37	16.72 ± 0.10	...	...
NGC 6093.....	−1.41	−1.21	16.12 ± 0.07	15.95 ± 0.10	...
NGC 6121.....	−1.19	−0.94	13.45 ± 0.10	13.40 ± 0.10	...
NGC 6171.....	−0.87	−0.70	15.70 ± 0.10	15.85 ± 0.05	...
NGC 6205.....	−1.39	−1.18	15.10 ± 0.15	14.75 ± 0.07	...
NGC 6218.....	−1.37	−1.17	14.75 ± 0.15	14.60 ± 0.07	...
NGC 6229.....	−1.30	−1.10	18.11 ± 0.05	18.00 ± 0.07	17.15 ± 0.05
NGC 6254.....	−1.41	−1.25	14.85 ± 0.10	14.65 ± 0.05	...
NGC 6266.....	−1.07	−0.87	16.40 ± 0.20	16.35 ± 0.05	...
NGC 6333.....	−1.56	−1.36	16.35 ± 0.15	15.95 ± 0.10	...
NGC 6341.....	−2.16	−1.95	15.30 ± 0.10	14.65 ± 0.05	...
NGC 6352.....	−0.64	−0.50	15.30 ± 0.10	...	...
NGC 6366.....	−0.87	−0.70	15.80 ± 0.10	...	14.75 ± 0.10
NGC 6397.....	−1.82	−1.65	13.00 ± 0.10	...	...
NGC 6440.....	−0.49	−0.40	18.70 ± 0.20	19.25 ± 0.05	...
NGC 6528.....	−0.38	−0.31	17.17 ± 0.20	17.95 ± 0.10	...
NGC 6535.....	−1.53	−1.33	15.90 ± 0.15	...	...
NGC 6553.....	−0.44	−0.36	16.92 ± 0.20	17.55 ± 0.10	...
NGC 6584.....	−1.30	−1.10	16.60 ± 0.05	16.40 ± 0.10	...
NGC 6637.....	−0.68	−0.55	15.95 ± 0.10	16.35 ± 0.07	...
NGC 6652.....	−0.87	−0.70	16.07 ± 0.10	...	...
NGC 6681.....	−1.27	−1.07	15.85 ± 0.10	15.65 ± 0.05	...
NGC 6712.....	−0.88	−0.71	16.32 ± 0.07	16.55 ± 0.05	...
NGC 6717.....	−1.10	−0.90	15.75 ± 0.15	15.75 ± 0.10	...
NGC 6752.....	−1.42	−1.21	13.90 ± 0.15	13.65 ± 0.05	...
NGC 6809.....	−1.61	−1.41	14.60 ± 0.10	14.15 ± 0.05	...
NGC 6838.....	−0.70	−0.49	14.52 ± 0.10	14.80 ± 0.15	...
NGC 6934.....	−1.30	−1.10	16.97 ± 0.07	16.85 ± 0.05	...
NGC 6981.....	−1.30	−1.10	16.86 ± 0.07	16.75 ± 0.07	...
NGC 7006.....	−1.35	−1.15	18.85 ± 0.15	18.55 ± 0.07	...
NGC 7078.....	−2.12	−1.91	15.90 ± 0.07	15.25 ± 0.05	...
NGC 7099.....	−1.91	−1.71	15.30 ± 0.10	...	...
NGC 7492.....	−1.27	−1.07	17.78 ± 0.10	17.55 ± 0.10	...
IC 4499	−1.26	−1.06	17.70 ± 0.07	...	...
Rup 106	−1.70	−1.50	17.85 ± 0.10	...	...
Arp 2.....	−1.64	−1.44	18.30 ± 0.15	...	...
Ter 7	−0.64	−0.52	17.87 ± 0.10	...	...
Ter 8	−1.60	−1.40	18.15 ± 0.10	17.65 ± 0.10	...

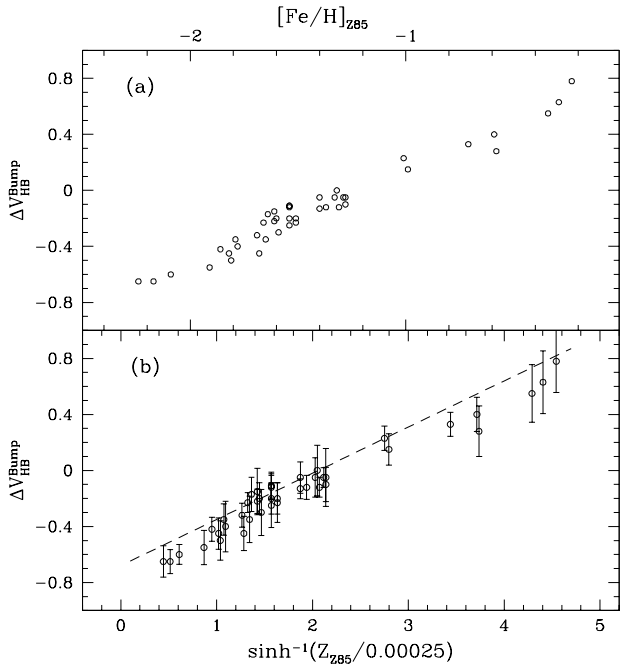

FIG. 12.—The parameter ΔV_{HB}^{bump} as a function of (*a*) metallicity ([Fe/H]$_{Z85}$) and (*b*) the parameter *s*. The dashed line is the relation obtained by F90.

predicted luminosity level of the RGB bump (see, e.g., Table 4 in SCL97). In addition, larger core masses at the He flash are now obtained, so that the predicted HB luminosity is higher than those found in the old computations. On the basis of the RGB and HB models described in § 4, we have derived the following relations for the RGB bump location and the ZAHB level:

$$M_V^{bump} = 0.7502 + 0.9896 \log t_9 + 1.5797[M/H] + 0.2574[M/H]^2 , \quad (3)$$

$$M_V^{ZAHB} = 1.0005 + 0.3485[M/H] + 0.0458[M/H]^2 , \quad (4)$$

where t_9 is the age in Gyr.

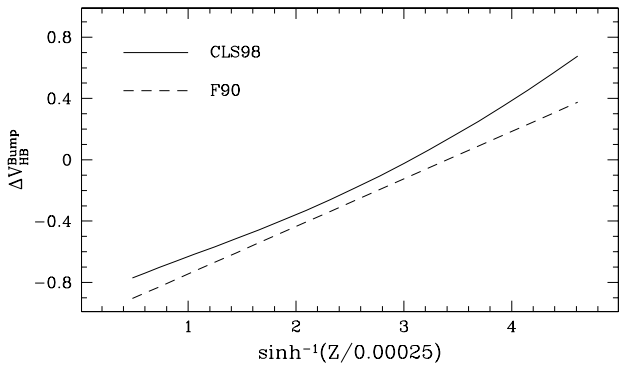

FIG. 13.—New and old theoretical ΔV_{HB}^{bump} as function of *s*: present models from CLS98 (*solid line*) and the relation adopted by F90 (*dashed line*).

In order to make easy the comparison with other published relations for the ZAHB level as a function of the metallicity, it could be useful to give here also the linear best-fit regression in the range $-0.4 < [M/H] < -2.2$:

$$M_V^{ZAHB} = 0.23[M/H] + 0.94 . \quad (5)$$

In Figure 13, we show a comparison between the old theoretical values (adopted by F90) for the ΔV_{HB}^{bump} parameters and the latest ones. The new values are significantly larger, by about 0.15–0.20 mag (up to 0.3 mag at the highest metallicity). Results from the new models are compared with the present data in Figure 14. We show the theoretical expectations for two different ages, 12 and 16 Gyr, which are roughly representative of the range of ages covered by the bulk of the Galactic globular clusters. The "old" (Z85) and the "new" (CG97) metallicity scales are shown in Figures 14*a* and 14*b*, respectively. Finally, in Figure 14*c* we adopt the *global* metallicity ([M/H]). Note that only in this third case is a good agreement between the theory and the observations obtained. The previous discrepancy of about 0.4 mag between theory and observation has been completely removed. The major changes are

1. The updated input physics in the evolutionary models, which yields an RGB bump less luminous (by

TABLE 6

RGB BUMP PARAMETERS AND THEIR CALIBRATION IN TERMS OF THE DIFFERENT METALLICITY SCALES

No.	Relation	Fit
	The Zinn Scale [Fe/H]$_{Z85}$	
(6.1).....	$\Delta V_{HB}^{bump} = 0.31 s_{Z85} - 0.72$	$n = 42$, $\sigma = 0.07$
(6.2).....	$\Delta V_{HB}^{bump} = 0.67[Fe/H]_{Z85} + 0.827$	$n = 42$, $\sigma = 0.06$
	The Carretta-Gratton Scale [Fe/H]$_{CG97}$	
(6.3).....	$\Delta V_{HB}^{bump} = 0.041 s_{CG97}^2 + 0.172 s_{CG97} - 0.753$	$n = 42$, $\sigma = 0.06$
(6.4).....	$\Delta V_{HB}^{bump} = 0.269[Fe/H]_{CG97}^2 + 1.451[Fe/H]_{CG97} + 1.220$	$n = 42$, $\sigma = 0.06$
	The Global Scale [M/H]	
(6.5).....	$\Delta V_{HB}^{bump} = 0.065 s^2 + 0.025 s_{global} - 0.702$	$n = 42$, $\sigma = 0.07$
(6.6).....	$\Delta V_{HB}^{bump} = 0.360[M/H]^2 + 1.602[M/H] + 1.113$	$n = 42$, $\sigma = 0.07$
	The Bump Location in the Absolute Plane M_V^{bump}	
(6.7).....	$M_V^{bump} = 0.29[Fe/H]_{CG97}^2 + 1.736[Fe/H]_{CG97} + 2.23$	$n = 42$, $\sigma = 0.06$
(6.8).....	$M_V^{bump} = 0.406[M/H]^2 + 1.95[M/H] + 2.113$	$n = 42$, $\sigma = 0.06$

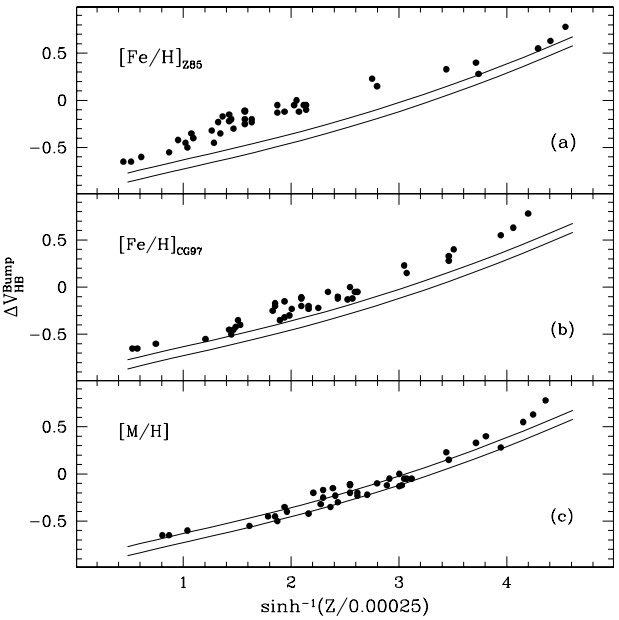

FIG. 14.—Same as Fig. 12, but for the three different metallicity scales: Zinn (1985, *top*), Carretta & Gratton (1997, *middle*), and global metallicity [M/H] (*bottom*). The two solid lines represent the theoretical predictions for two different ages, namely, 12 Gyr (*lower line*) and 16 Gyr (*upper line*).

$\sim$0.1–0.15 mag) because of the increased opacity, and an HB level more luminous (by $\sim$0.05 mag) because of increased core mass;

2. The new spectroscopic abundances ([α/Fe] and [Fe/H]), which contribute $\sim$0.2 mag; and

3. The new definition of the HB level, which contributes $\sim$0.05–0.1 mag.

The best-fit relations obtained in terms of the different metallicity scales are listed in Table 6. For each metallicity scale the behavior of the ΔV_{HB}^{bump} parameter has been computed both in terms of the usual metallicity parameter ([Fe/H], [M/H], etc.) and the parameter s defined by F90.

7. THE ASYMPTOTIC GIANT BRANCH

According to the evolutionary models (Castellani, Chieffi, & Pulone 1991), after the exhaustion of the central He, the He burning rapidly moves from the center toward the maximum mass coordinate attained by the convective core during the HB phase. Thus, the beginning of the AGB is characterized by a rapid increase in luminosity. When the shell He burning stabilizes, a slowing down of the evolutionary rate is expected. Then, from an observational point of view, the transition between the central and the shell He burning should be marked by a clear gap (where few stars should be found), while a well-defined clump of stars should indicate the base of the AGB.

It has been recognized (Castellani et al. 1991; Pulone 1992; Bono et al. 1995) that the luminosity level of the AGB clump is almost independent of the chemical composition of the cluster stars (both Z and Y), so that this (quite bright) feature could be a very promising "standard candle." However, we note that the theoretical calibration of the AGB clump location is affected by the uncertainties in the actual extension of the convective core of an He-burning low-mass star. On the other hand, as pointed out by Caputo et al. (1989), one might use the observed differences between the HB luminosity level and that of the AGB clump (i.e., $\Delta V_{AGB}^{HB} = V_{clump}^{AGB} - V_{HB}$) to constrain the convection theory (instability criterion, semiconvection, overshooting, and the like; see Dorman & Rood 1993).

Unfortunately, the identification of such a clump is not easy, since the AGB phase itself is very short ($\sim 10^7$ yr) and, in turn, always poorly populated (a GGC with total luminosity $L_T = 10^5\ L_\odot$ contains $\sim$20 AGB stars; see Renzini & Fusi Pecci 1988). There are a few identifications of the AGB clump in the literature: Ferraro (1992) reported a preliminary identification of this feature in three GGCs (M5, NGC 1261, NGC 2808), and Montegriffo et al. (1995) showed that it is clearly visible in 47 Tuc. Other examples could be found in published CMDs, but the AGB clump detection has been neither noted nor discussed.

To initiate a systematic study of the properties of the AGB clump, we have independently identified such a feature in nine GGCs whose CMDs show a significant clump of stars in the AGB region. In Table 5 (col. [6]), the apparent V magnitudes of the approximate centroid of the AGB clump stars' distribution is listed for each of these nine clusters.

In order to study the behavior of the AGB clump from a theoretical point of view, a subset of CLS98 models was evolved through the onset of He shell burning up to the first thermal pulse. The main results are presented in Figure 15, where the absolute V magnitude of the AGB clump is plotted versus the ZAHB mass, for two different metallicities ($\log Z = -3$ and $\log Z = -4$). The corresponding $B-V$ colors of the AGB clump are also reported for each model. Both the color and the luminosity of the AGB clump depend significantly on the stellar mass (see also Fig. 2 of Castellani, Chieffi, & Pulone 1989). In particular, higher stellar masses tend to generate brighter and redder AGB clumps. Thus, in principle, the dependence of the AGB clump luminosity on the mass of the evolving star implies, in turn, an indirect dependence on all the other parameters that could affect the mean mass (and its distribution) along the HB: namely, metallicity, age, mass-loss efficiency, and all the parameters that directly or indirectly affect the mass-loss process. However, it is interesting to note that for low-metallicity clusters (but in general for clusters with blue

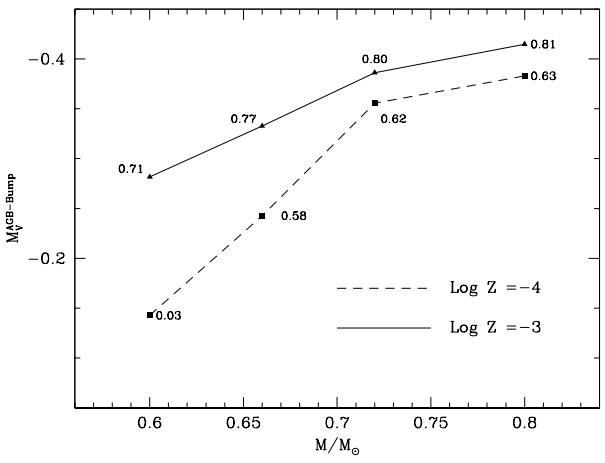

FIG. 15.—Theoretical luminosity level of the AGB clump as function of stellar mass for two metallicities, namely, $Z = 0.0001$ and $Z = 0.001$ (*dashed and solid line, respectively*). The labels reported in the figure are the $B-V$ colors of the computed AGB clumps.

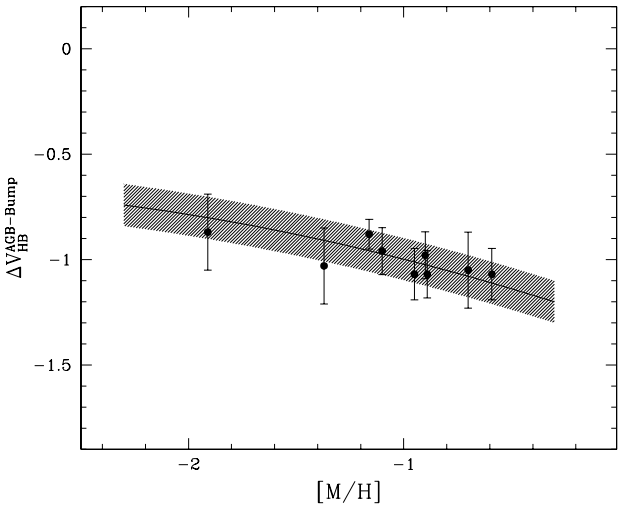

FIG. 16.—Difference between the observed ZAHB and AGB clump luminosity levels of nine clusters in our catalog. The solid line is the theoretical expectation. The hatched region is representative of the uncertainty (± 0.1 mag) in the absolute location of the AGB clump (see text).

HBs), the AGB clump rapidly tends to become bluer and bluer (up to $B-V \sim 0.0$) and probably (because the spread in mass along the ZAHB) progressively less *clumpy* and, for this reason, less observable. This effect is nicely shown, for example, by Figure 4 of Rood, Whitney, & D'Cruz (1997) and Figure 8 of Whitney et al. (1998). Thus, operatively, whether the AGB clump is observable or not determines to some extent the possible range in luminosity that might be observable for this feature. The models suggest that observable AGB bumps are located at $M_V^{\rm AGBbump} = -0.3 \pm 0.1$.

In Figure 16, we compare the theoretical and observed values of the $\Delta V_{\rm HB}^{\rm AGB}$ parameter. The hatched region represents the quoted uncertainty (± 0.1) in the absolute location of the AGB clump. Despite the quite large error bar affecting most of the (few) available measurements of the AGB clump, the level of the agreement with the theoretical prediction is remarkable. Such a result, especially combined with that obtained in § 6.4 for the RGB bump location, is comforting as to the reliability and the internal consistency of the adopted theoretical prescriptions.

For the sake of completeness we give below the best-fit relation for the $\Delta V_{\rm HB}^{\rm AGB}$ parameter as a function of the metallicity in the CG97 and the global metallicity scale, respectively:

$$\Delta V_{\rm HB}^{\rm AGB} = -0.16[{\rm Fe/H}]_{\rm CG97} - 1.19 \quad (n = 9,\ \sigma = 0.06)\ , \tag{6}$$

$$\Delta V_{\rm HB}^{\rm AGB} = -0.17[{\rm M/H}] - 1.17 \quad (n = 9,\ \sigma = 0.05)\ . \tag{7}$$

8. TOWARD ABSOLUTE QUANTITIES

In order to carry out an exhaustive comparison with the models, we have to derive *absolute* quantities from our data. This implies the knowledge (or the assumption) of a "reliable" distance scale for the program clusters. As is well known (see, e.g., the recent discussion by Gratton et al. 1997 and Carretta et al. 1999), different loci in the CMD and different standard candles can be assumed to determine the distance to a given cluster (see also Cacciari 1999 for an extensive review). Here we adopt just a *given* standard candle and briefly comment on the possible impact of alternative choices. Any variation in the zero point or of the metallicity dependence of the luminosity of the adopted candles would in fact affect the conclusions.

Since our study is mainly devoted to the quantitative analysis of the evolved sequences (including the HB), it is quite natural to adopt HB stars as standard candles, at least for heuristic purposes. Unfortunately, although the HB is the *classical* sequence traditionally used as reference branch, there is still strong disagreement on the basic *absolute* calibration. For the sake of discussion, in the following we will use our theoretical ZAHB as standard candle, as this choice guarantees complete self-consistency in our approach. We leave to future studies the assessment of the validity of the HB models as suitable candles. We discarded here the use of empirical relations since none of those presented so far (see for references VandenBerg, Stetson, & Bolte 1996; Gratton et al. 1997; Reid 1997, 1998; Cacciari 1999) actually calibrate the "true" ZAHB level, but rather adopt the mean apparent magnitude of the HB at a given color, $\langle V_{\rm HB} \rangle$, or an empirically derived ZAHB level, obtained from the mean HB level via some metallicity- and HB morphology–dependent correction factors.

The distance moduli were computed by adopting as reference equation (4) from § 6.4. Values were computed using both the metallicity scale from the spectroscopic iron abundance measurements (GC97) and the global metallicity scale (as derived in § 3). Note that the adoption of the CG97 spectroscopic scale rather than the Z85 scale leads to an average decrease of the absolute luminosity of the ZAHB level and, in turn, of the derived distance scale by ~ 0.03. An additional decrease in luminosity (~ 0.04 mag) occurs if α-enhancements are included to obtain the global metallicity ([M/H]).

The distance moduli obtained assuming $[{\rm Fe/H}]_{\rm CG97}$ and [M/H] are listed in Table 2, columns (7) and (8), respectively. Note that in computing the DM we adopted the individual reddening as listed in column (5) of Table 2. Considering that the derived DMs are affected by many uncertainties (namely, the evaluation of the ZAHB level, the zero point and dependence on metallicity of the ZAHB level, reddening, etc.), we estimate that the global uncertainty affecting the DMs listed in Table 2 cannot be less than 0.2 mag.

These values can be then compared with those reported in the two most recent compilations of GGC observable parameters, Djorgovski (1993) and Harris (1996), which were, however, derived under assumptions significantly different from those adopted here. In fact, Djorgovski (1993) assumed a constant value for the HB level ($M_V^{\rm HB} = 0.6$) independent of metallicity, while Harris (1996) adopted $M_V^{\rm HB} = 0.20[{\rm Fe/H}] + 1.0$, based on the empirical relation obtained by Carney et al. (1992).

The residuals for the DM (this minus previous paper) as a function of $[{\rm Fe/H}]_{\rm CG97}$ are plotted in Figures 17*a* and 17*b*, for D93 and H96, respectively. In the comparison with D93, there is a clear trend of the residuals as a function of metallicity, mostly due to the assumption of a constant $M_V^{\rm HB}$. No similar trend is detectable with respect to H96, since the assumption on the slope of the $M_V^{\rm HB}$-[Fe/H] relation is compatible with that assumed here (see eq. [5]). There is, however, a clear systematic offset (~ 0.15–0.2), partially due

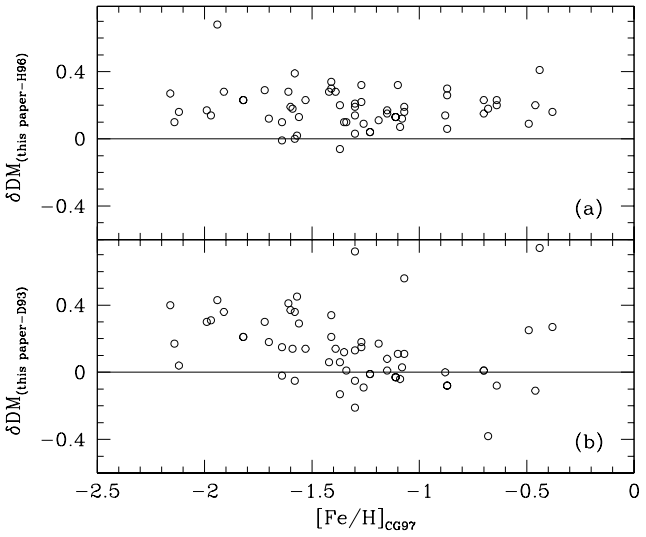

FIG. 17.—Difference between the DMs obtained in this paper and the previous compilations by (*a*) H96 and (*b*) D93. A systematic difference of ~0.2 mag is evident in the comparison with the H96 data. The trend with metallicity clearly evident in (*b*) is due to the D93 assumption on V_{HB} (see text).

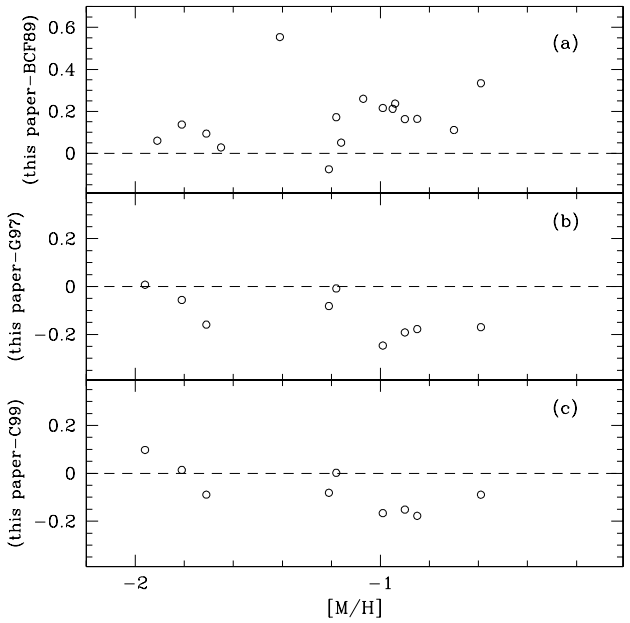

FIG. 18.—Difference between the DMs obtained in this paper and those obtained from (*a*) BCF89; (*b*) *Hipparcos* parallaxes (Gratton et al. 1997); (*c*) revised *Hipparcos* parallaxes (Carretta et al. 1999).

to the different zero point of the adopted relation and partially due to the difference in the procedure used to determine the level of the ZAHB (see § 5).

8.1. *Comparison with Other Empirical Distances*

As quoted in the previous section, an extensive comparison between the distance moduli obtained here and those derived by adopting different standard candles is beyond the purpose of the present paper. For the sake of example, in this section we report two among the most recent results obtained adopting different candles.

8.1.1. *The Main Sequence*

Among others, this approach was used by BCF89, who compared the observed main-sequence (MS) mean ridgelines for a sample of 19 GGCs with the reference locus defined by six local subdwarfs. From this procedure they derived distances and ages for the program clusters. The residuals of the comparison of the DM (this paper minus BCF89) are plotted as a function of metallicity ($[Fe/H]_{CG97}$) in Figure 18*a*. As can be seen the mean difference is ~0.15 mag, the DMs derived in this paper being systematically larger than those obtained by BCF89. The discrepancy (~0.6) found for NGC 6809 is due in part to the different photometry adopted here and in part to the different assumption about the reddening: BCF89 assumed 0.14, while here we used 0.07, from Harris 1996).

The same methodological approach has been followed recently by Gratton et al. (1997), who gave new distances for a sample of nine GGCs. These distances are based on high-precision trigonometric parallaxes for a sample of ~30 local subdwarfs from the *Hipparcos* satellite. They found that the derived distances for the selected sample of GGCs are systematically larger (~0.2 mag) than previously estimated. The residuals of the corresponding distances (this paper minus *Hipparcos*) are plotted as a function of metallicity ($[Fe/H]_{CG97}$) in Figure 18*b*. While there is agreement between our DMs and the *Hipparcos* DMs at the lowest metallicities, there seems to be a systematically increasing discrepancy as metallicity increases. The sample is certainly too poor to derive any firm conclusion.

However, it is interesting to note that the recent reanalysis of the *Hipparcos* data presented by Carretta et al. (1999) goes in the direction of showing a better agreement with the distances obtained in this paper; in Figure 17*c*, the residuals with respect to these most recent determinations have been plotted, and as can be seen, the distance determinations for clusters in the low-metallicity domain nicely agree, while some systematic difference still remains at the high-metallicity end. Since the difference in the distance modulus, of about 0.07 mag, implies a corresponding difference in age of about 1 Gyr, it is quite evident that the differences found for specific clusters are still high as far as the age determination is concerned. However, the sample is so small that it is still impossible to draw any reliable conclusion.

It is also important to bear in mind that because of the steepness of the MS, the "main-sequence fitting" method used to derive distances is strongly limited by any uncertainty affecting the MS colors (metallicity, reddening, photometry calibration, and the like) of both the clusters and the reference stars (subdwarfs).

8.1.2. *White Dwarfs*

The cooling sequence of white dwarfs has been used recently by Renzini et al. (1996) as a distance indicator to determine the distance of the nearby cluster NGC 6752. For this cluster they derived $(m - M)_0 = 13.05$, with an overall uncertainty of ± 0.1 mag. This value is compatible with the DM obtained using the global metallicity ([M/H]) $(m - M)_0 = 13.14 \pm 0.10$ (see col. [8] in Table 2).

8.2. *The Absolute Quantities*

Using the assumptions and results obtained in the previous sections for the distances, it is possible to obtain various interesting plots that describe in a very direct and

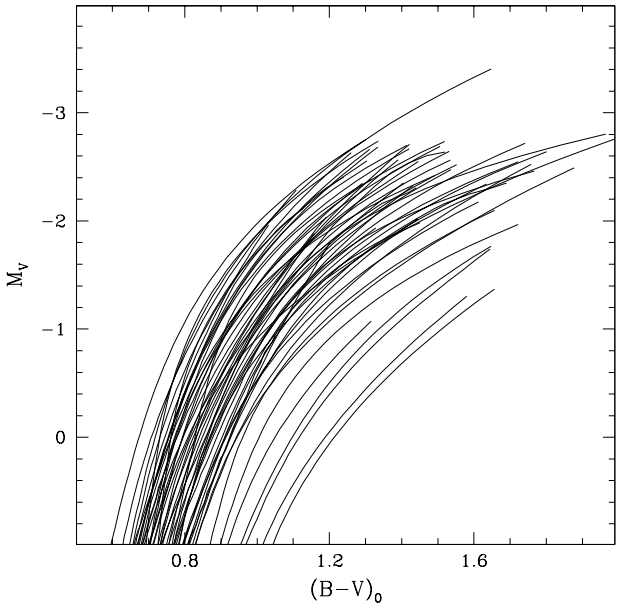

FIG. 19.—RGB mean ridgelines for 55 GGCs in the absolute plane $[M_V,(B-V)_0]$. The adopted DM as been computed assuming the metallicity in the CG97 scale (see text).

clear way the properties of the RGB (and in particular its location and morphology) with varying metallicity.

In Figure 19, we present the mean ridgeline for 55 GGCs in the absolute plane $[M_V,(B-V)_0]$. The DMs obtained from the $[Fe/H]_{CG97}$ scale have been adopted to construct the diagram. As can be noted from this figure, at least three clusters (namely, NGC 6333, 6535, and 7492) appear to cross over the other mean ridgelines, suggesting that photometry for these clusters could be affected by calibration

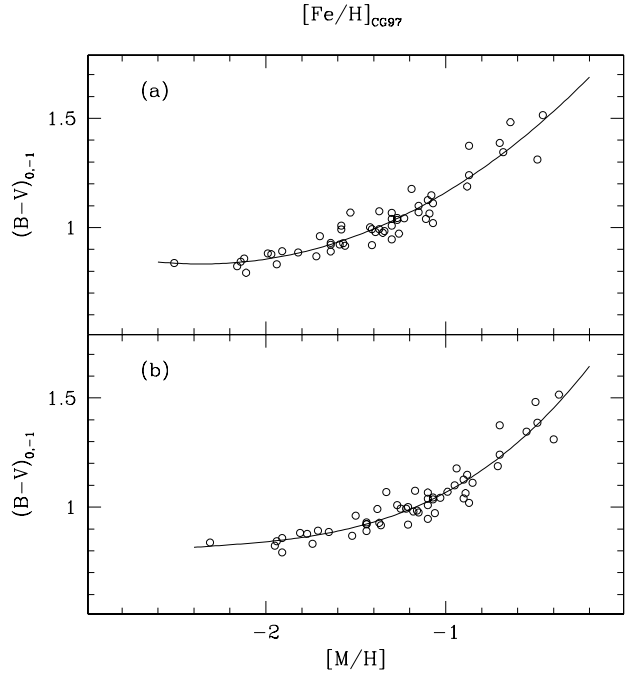

FIG. 20.—Intrinsic $(B-V)_0$ color of the RGB, measured at $M_V = -1$, as a function of (*a*) $[Fe/H]_{CG97}$ and (*b*) [M/H]. The solid lines are the best-fit relations listed in Table 4 (eqs. [4.15] and [4.16], respectively).

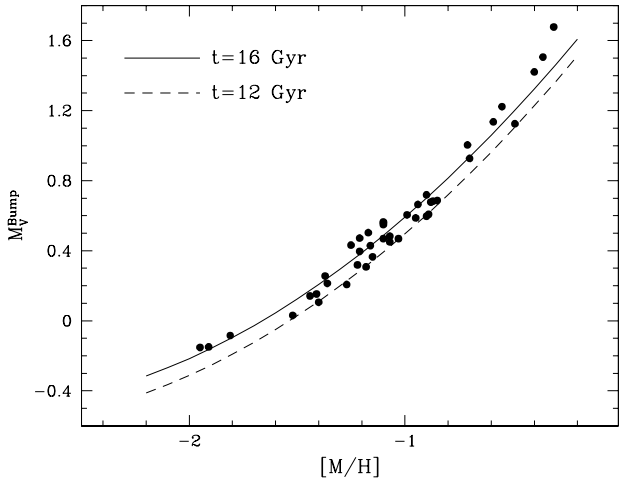

FIG. 21.—Absolute magnitude of the RGB bump as a function of the global metallicity [M/H] (the DM has been computed accordingly). The solid line is the theoretical prediction from CLS98 models at $t = 16$ Gyr; the dashed line represents the same set of models at $t = 12$ Gyr.

problems, and they deserve a more accurate photometric analysis.

Figures 20*a* and 20*b* report the intrinsic colors of the RGB measured at $M_V = -1$ [labeled as $(B-V)_{0,-1}$ and listed in the last column of Table 3] as a function of $[Fe/H]_{CG97}$ and [M/H], respectively. Also plotted are the best-fit relations reported in Table 4 (eqs. [4.15] and [4.16]).

Figure 21 shows the dependence of the absolute location of the RGB bump on the global metallicity. For comparison with theoretical expectations, the relation from SCL97 has been overplotted at two different ages (as in the previous figure), at 16 Gyr (*solid line*) and 12 Gyr (*dashed line*). As can be seen from this figure, the previous discrepancy between the observation and the model prediction for the location of this feature is completely removed by using the new models and considering the global metallicity scale (as expected from the discussion in § 6.4). Finally, analytic relations giving the absolute magnitude of the RGB bump as a function of the metallicity using both the CG97 and the global scale have been computed. They are listed in Table 6 (eqs. [6.7] and [6.8]).

Though intriguing in principle, the uncertainty on the data is still too large to allow any attempt to derive information on a possible age spread within the GGC system from such a data set.

9. FINAL REMARKS ON THE METALLICITY ASSUMPTIONS

In this section we briefly discuss the effects of adopting different assumptions for the metallicity on the relations we derived in the previous sections, in particular,

1. The use of the metal abundance ([Fe/H]) estimates obtained by RHS97 in the CG97 scale instead of those listed in column (3) of Table 1; and
2. The adoption of the Carney (1996) scenario for the α-element enhancing relation (see Fig. 2*b*), rather than that plotted in Figure 2*a*, in computing the global metallicity.

1. As already shown in Figure 1*b*, the metal abundance obtained by RHS97 in the CG97 scale for the 42 GGCs in

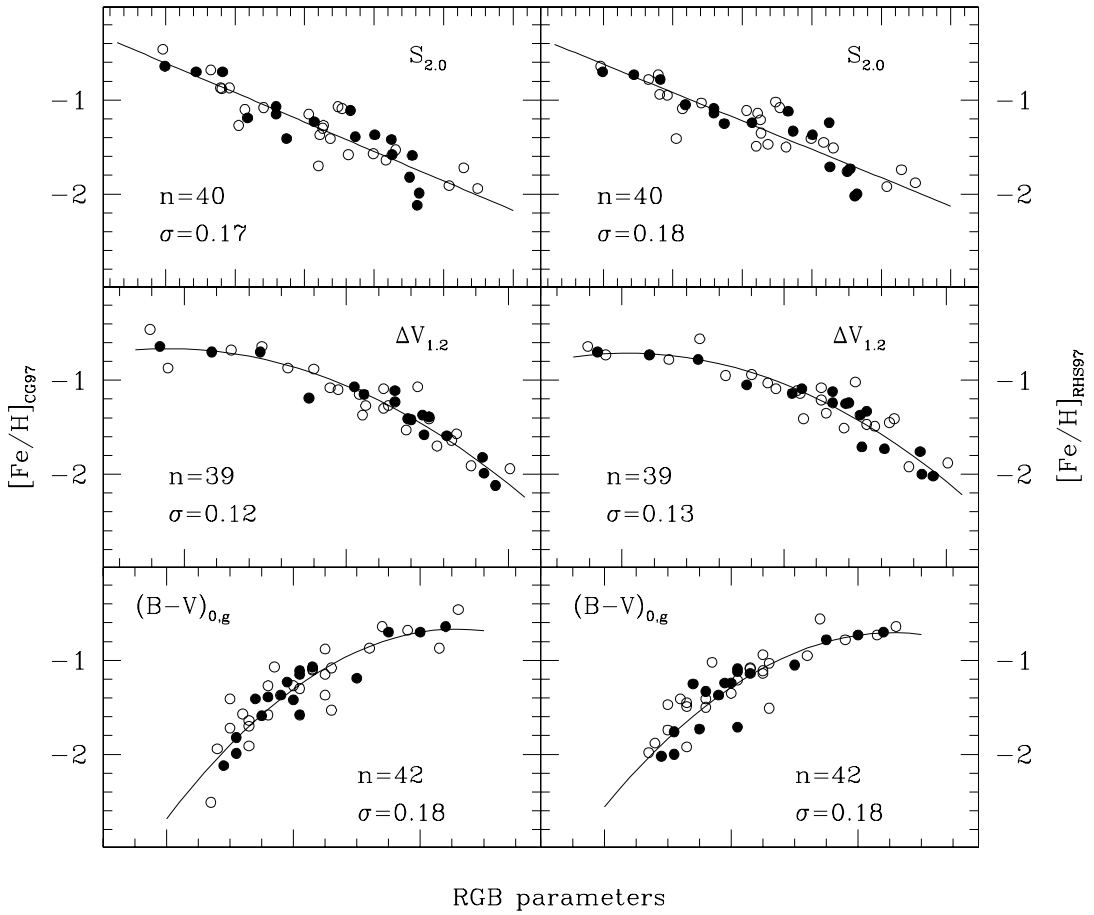

FIG. 22.—$[Fe/H]_{CG97}$ vs. the values obtained for three RGB parameters defined in § 6.2 [namely, $S_{2.0}$, $\Delta V_{1.2}$, $(B-V)_{0,g}$] as computed in § 3.2 (*left*) and by RHS97 (*right*). The number of clusters used to compute each relation is reported, together with the standard deviations of the data. In order to compute the scatter in a homogeneous way, only clusters in common with the RHS97 list have been considered in the plots on the left.

common is fully compatible (within 0.2 dex) with that adopted in this paper (computed following the procedure described in § 3.2). For this reason we expect very little effect on the relations we derived in the previous sections. For the sake of example, in Figure 22 we report the results for the relations we obtained for three of the RGB parameters we defined in § 6.2 [namely, $S_{2.0}$, $\Delta V_{1.2}$, $(B-V)_{0,g}$]. In the left panels of Figure 21 we plot the relations obtained assuming $[Fe/H]_{CG97}$ listed in Table 1, in the right panels those assuming the values listed by RHS97. The number of clusters used to compute each relation is shown in each panel together with the standard deviation of the data. In order to properly compare the scatter of the data with respect to the best-fit relation under the same assumptions, only clusters in common between our sample and RHS97 have been used. As can be seen from the comparisons between each pair of panels, the results are fully compatible both in terms of fit relations and data scatter.

2. In Figure 2*a* we plotted the α-element enhancing relation adopted to compute the global metallicity listed in column (4) of Table 1. However, as discussed in § 3.4, the trend of the [α/Fe] as a function of [Fe/H], at least for GGCs, is still very uncertain, especially in the high-metallicity domain. For this reason we show the effects of different assumptions in the α-enhancing relation on our

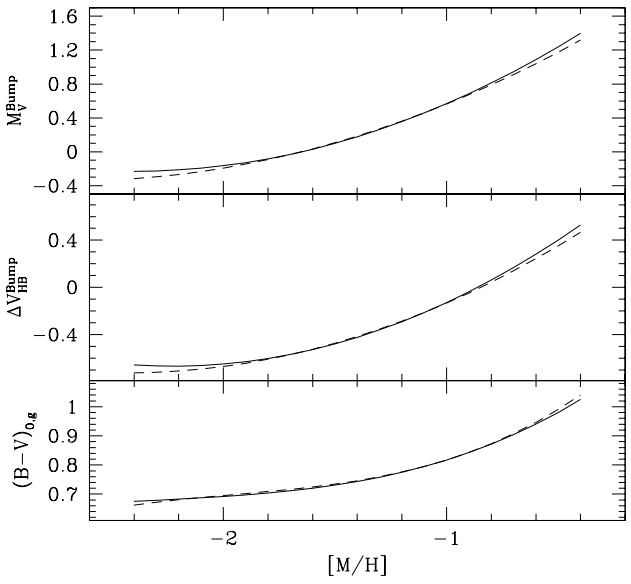

FIG. 23.—$(B-V)_{0,g}$, ΔV_{HB}^{bump}, and M_V^{bump} as functions of the global metallicity, computed by adopting the α-enhancement relation plotted in Fig. 1*a* (*solid lines*) and adopting the α-enhancement scenario proposed by Carney (1996) plotted in Fig. 1*b* (*dashed lines*). As can be seen, the two different assumptions have a very small effect on the derived relations.

results. We adopted the scenario proposed by Carney (1996) and plotted in Figure 2*b*. Even in this case, for the sake of example, in Figure 23 we plotted three relations obtained in the previous sections [respectively for $(B-V)_{0,g}$, ΔV_{HB}^{bump}, and M_V^{bump}] as a function of the global metallicity computed adopting the two different scenarios. In particular, solid lines are the best-fit relation obtained using the global metallicity listed in Table 2, while dashed lines are computed adopting the Carney (1996) scenario. As can be seen, only a small effect is visible at the extreme ends of the relations, as expected, since the assumption of the Carney (1996) scenario only slightly increases (on average by 0.07 dex, the maximum being 0.13 dex) the global metallicity for metal-rich ($[Fe/H]_{CG97} < -1$) clusters (13 in our sample).

In summary, we can reasonably conclude that the relations derived in this paper are little affected by the assumptions we adopted for the metallicity.

10. CONCLUSIONS AND FUTURE PROSPECTS

A careful revision of all the best available CMDs for the post–main-sequence branches (RGB, HB, AGB) of GGCs has allowed us to build a wide data set. A variety of observables quantitatively describing the main properties of the considered branches as far as the location and the basic features in the CMDs were measured: the various quantities obtained via a homogeneous procedure applied to each individual CMD have been examined by varying the cluster metallicity, also taking into account the effects of α-enhancements, and compared with the predictions of theoretical models. Very schematically this comparison has shown a substantial agreement between observations and theoretical predictions, with a significant improvement with respect to any similar previous study. The basic items that contribute to this result are (1) the availability of a carefully tested, wide sample of clusters (61); (2) the adoption of an innovative, homogeneous procedure to estimate the ZAHB level; (3) the adoption of new metallicity scales; and (4) the comparison with updated, self-consistent models.

Further significant improvements in the analysis could eventually be made, as soon as new data for other clusters become available and, in particular, when more accurate estimates on the global metal content ([Fe/H] and α-elements) of GGC stars are obtained via high-resolution spectroscopy and new, more accurate absolute distance moduli measured via alternative, complementary methods.

We warmly thank a dear friend (Bob Rood) for a careful reading of the manuscript. The financial support of the Ministero della Università e della Ricerca Scientifica e Tecnologica (MURST) to the project Stellar Evolution is kindly acknowledged. F. R. F. acknowledges the ESO visitor program for its hospitality.

REFERENCES

Alexander, D. R., & Ferguson, J. W. 1994, ApJ, 437, 879
Alongi, M., Bertelli, G., Bressan, A., & Chiosi, C. 1991, A&A, 244, 95
Armandroff, T. E., & Zinn, R. 1988, AJ, 96, 92
Beaudet, G., Petrosian, V., & Salpeter, E. E. 1967, ApJ, 150, 979
Bergbusch, P. A. 1993, AJ, 106, 1024
———. 1996, AJ, 112, 1061
Bessell, M. S., Castelli, F., & Plez, B. 1998, A&A, 333, 231 (erratum 337, 321)
Bono, G., Castellani, V., Degl'Innocenti, S., & Pulone, L. 1995, A&A, 297, 115
Bordoni, M. A. 1995, Master's thesis, Bologna Univ.
Borissova, J., Catelan, M., Ferraro, F. R., Spassova, N., Buonanno, R., Iannicola, G., Richtler, T., & Sweigart, A. V. 1999, A&A, 343, 813
Borissova, J., Catelan, M., Spassova, N., & Sweigart, A. V. 1997, AJ, 113, 692
Brocato, E., Buonanno, R., Malakhova, Y., & Piersimoni, A. M. 1996, A&A, 311, 778
Brocato, E., Castellani, V., & Ripepi, V. 1995, AJ, 109, 1670
Brocato, E., Castellani, V., Scotti, G. A., Saviane, I., Piotto, G., & Ferraro, F. R. 1998, A&A, 335, 929
Buonanno, R., Caloi, V., Castellani, V., Corsi, C., Fusi Pecci, F., & Gratton, R. 1986, A&AS, 66, 79
Buonanno, R., Corsi, C., Bellazzini, M., Ferraro, F. R., & Fusi Pecci, F. 1997, AJ, 113, 706
Buonanno, R., Corsi, C. E., Buzzoni, A., Cacciari, C., Ferraro, F. R., & Fusi Pecci, F. 1994, A&A, 290, 69
Buonanno, R., Corsi, C. E., Ferraro, I., & Fusi Pecci, F. 1987, A&AS, 67, 327
Buonanno, R., Corsi, C. E., & Fusi Pecci, F. 1981, MNRAS, 196, 435
———. 1985, A&A, 145, 97
———. 1989, A&A, 216, 80 (BCF89)
Buonanno, R., Corsi, C. E., Fusi Pecci, F., Alcaino, G., & Liller, W. 1984, A&AS, 57, 75
Buonanno, R., Corsi, C. E., Fusi Pecci, F., Richer, H. B., & Fahlman, G. G. 1993, AJ, 105, 184
———. 1995a, AJ, 109, 650
Buonanno, R., Corsi, C. E., Pulone, L., Fusi Pecci, F., Richer, H. B., & Fahlman, G. G. 1995b, AJ, 109, 663
Buonanno, R., Fusi Pecci, F., Cappellaro, E., Ortolani, S., Richtler, T., & Geyer, E. H. 1991, AJ, 102, 1005
Buzzoni, A., Fusi Pecci, F., Buonanno, R., & Corsi, C. E. 1983, A&A, 128, 94
Cacciari, C. 1999, in ASP Conf. Ser. 167, Harmonizing Cosmic Distance Scales in a Post-*Hipparcos* Era, ed. D. Egret & A. Heck (San Francisco: ASP), 140
Caputo, F., Castellani, V., Chieffi, A., Pulone, L., & Tornambè, A. 1989, ApJ, 340, 241
Carney, B. W. 1996, PASP, 108, 900
Carney, B. W., Fullton, L. K., & Trammell, S. R. 1991, AJ, 101, 1699
Carney, B. W., Storm, J., & Jones, R. V. 1992, ApJ, 386, 663
Carretta, E., & Bragaglia, A. 1998, A&A, 329, 937
Carretta, E., & Gratton, R. G. 1997, A&AS, 121, 95 (CG97)
Carretta, E., Gratton, R. G., Clementini, G., Fusi Pecci, F. 1999, ApJ, submitted (astro-ph/9902086)
Cassisi, S., & Salaris, M. 1997, MNRAS, 285, 593
Castellani, V., Chieffi, A., & Pulone, L. 1989, ApJ, 344, 239
———. 1991, ApJS, 76, 911
Castellani, V., Chieffi, A., Pulone, L., & Tornambè, A. 1985, ApJ, 294, L31
Castellani, V. & Tornambè, A. 1977, A&A, 61, 427
Caughlan, G. R., & Fowler, W. A. 1988, At. Data Nucl. Data Tables, 40, 283
Caughlan, G. R., Fowler, W. A., Harris, M. J., & Zimmerman, B. A. 1985, At. Data Nucl. Data Tables, 32, 197
Chaboyer, B., Demarque, P., & Sarajedini, A. 1996, ApJ, 459, 558
Chieffi, A., Limongi, M., & Straniero, O. 1998a, in preparation (CLS98)
Chieffi, A., & Straniero, O. 1989, ApJS, 71, 47
Chieffi, A., Straniero, O., & Limongi, M. 1998b, in preparation
Christian, C. A., & Heasley, J. N. 1988, AJ, 95, 1422
Cohen, J. G. 1983, ApJ, 270, 654
Covino, S., & Ortolani, S. 1997, A&A, 318, 40
Cudworth, K. M. 1985, AJ, 90, 65
———. 1988, AJ, 96, 105
Desidera, S. 1996, Master's thesis, Padua Univ.
Dicus, D. A., Kolb, E. W., Schramm, D. N., & Tubbs, D. L. 1976, ApJ, 210, 481
Djorgovski, S. 1993, in ASP Conf. Ser. 50, Structure and Dynamics of Globular Clusters, ed. S. G. Djorgovski & G. Meylan (San Francisco: ASP), 373
Dorman, B., & Rood, R. T. 1993, ApJ, 409, 387
Edvardsson, B., Andersen, J., Gustafsson, B., Lambert, D. L., Nissen, P. E., & Tomkin, J. 1993, A&A, 275, 101
Ferraro, F. R. 1992, Mem. Soc. Astron. Italiana, 63, 491
Ferraro, F. R., Carretta, E., Corsi, C. E., Fusi Pecci, F., Cacciari, C., Buonanno, R., Paltrinieri, B., & Hamilton, D. 1997a, A&A, 320, 757
Ferraro, F. R., Clementini, G., Fusi Pecci, F., & Buonanno, R. 1991, MNRAS, 252, 357
Ferraro, F. R., Clementini, G., Fusi Pecci, F., Buonanno, R., & Alcaino, G. 1990, A&AS, 84, 59
Ferraro, F. R., Clementini, G., Fusi Pecci, F., Sortino, R., & Buonanno, R. 1992a, MNRAS, 256, 391
Ferraro, F. R., Clementini, G., Fusi Pecci, F., Vitiello, E., & Buonanno, R. 1993a, MNRAS, 264, 273
Ferraro, F. R., Fusi Pecci, F., & Bellazzini, M. 1995a, A&A, 294, 80
Ferraro, F. R., Fusi Pecci, F., & Buonanno, R. 1992b, MNRAS, 256, 376
Ferraro, F. R., Fusi Pecci, F., Cacciari, C., Corsi, C. E., Buonanno, R., Fahlman, G. G., & Richer, H. B. 1993b, AJ, 106, 2324

Ferraro, F. R., Fusi Pecci, F., Guarnieri, M. D., Moneti, A., Origlia, L., & Testa, V. 1994, MNRAS, 266, 829
Ferraro, F. R., Paltrinieri, B., Fusi Pecci, F., Cacciari, C., Dorman, B., & Rood, R. T. 1997b, ApJ, 484, L145
Ferraro, F. R., et al. 1997c, A&A, 324, 915
Ferraro, F. R., Paltrinieri, B., Fusi Pecci F., Rood, R. T., & Dorman, B. 1998, ApJ, 500, 311
Ferraro, F. R., Paltrinieri, B., Rood, R. T., & Dorman, B. 1999, ApJ, 522, 980
Ferraro, I., Ferraro, F. R., Fusi Pecci, F., Corsi, C. E., & Buonanno R. 1995b, MNRAS, 275, 1057
Fusi Pecci, F., Ferraro, F. R., Bellazzini, M., Djorgovski, S., Piotto, G., & Buonanno, R. 1993, AJ, 105, 1145
Fusi Pecci, F., Ferraro, F. R., Corsi, C. E., Cacciari, C., & Buonanno, R. 1992, AJ, 104, 1831
Fusi Pecci, F., Ferraro, F. R., Crocker, D. A., Rood, R. T., & Buonanno, R. 1990, A&A, 238, 95 (F90)
Gratton, R., Carretta, E., Matteucci, F., & Sneden, C. 1996, in ASP Conf. Ser. 92, The Formation of the Galactic Halo... Inside and Out, ed. H. L. Morrison & A. Sarajedini (San Francisco: ASP), 307
Gratton, R. G., Fusi Pecci, F., Carretta, E., Clementini, G., Corsi, C. E., & Lattanzi, M. 1997, ApJ, 491, 749
Harris, W. E. 1982, ApJS, 50, 573
———. 1996, AJ, 112, 1487 (H96)
Harris, W. E., Racine, R., & de Roux, J. 1976, ApJS, 31, 13
Hartwick, F. D. A. 1968, ApJ, 154, 475
Hesser, J. E., Harris, W. E., VandenBerg, Allwright, J. W. E., Shott, P., & Stetson, P. B. 1987, PASP, 99, 739
Iben, I., Jr. 1968, Nature, 220, 143
Iglesias, C. A., Rogers, F. J., & Wilson, B. G. 1992, ApJ, 397, 717
Itoh, N., Mitake, S., Iyetomi, H., & Ichimaru, S. 1983, ApJ, 273, 774
Kaluzny, J. 1997, A&AS, 122, 1
King, C. R., Da Costa, G. S., & Demarque, P. 1985, ApJ, 299, 674
Janes, K. A., & Heasley, J. N. 1991, AJ, 101, 2097
Lee, S.-W. 1977, A&AS, 28, 409
Lee, Y.-W., Demarque, P., & Zinn, R. 1990, ApJ, 350, 155
Magain, P. 1989, A&A, 209, 211
Momany, Y. 1996, Master's thesis, Bologna Univ.
Montegriffo, P., Ferraro, F. R., Fusi Pecci, F., & Origlia, L. 1995, MNRAS, 276, 739
Munakata, H., Kohyama, Y., & Itoh, N. 1985, ApJ, 296, 197 (erratum 304, 580 [1986])
Nissen, P. E., Gustafsson, B., Edvardsson, B., & Gilmore, G. 1994, A&A, 285, 440
Ortolani, S., Barbuy, B., & Bica, E. 1994a, A&AS, 108, 653
Ortolani, S., Bica, E., & Barbuy, B. 1994b, A&A, 286, 444
Ortolani, S., & Gratton, R. 1990, A&AS, 82, 71
Ortolani, S., Renzini, A., Gilmozzi, R., Marconi, G., Barbuy, B., Bica, E., & Rich, R. M. 1995, Nature, 377, 701
Paltrinieri, B., Ferraro, F. R., Fusi Pecci, F., & Carretta, E. 1998, MNRAS, 293, 434
Pike, C. D. 1976, MNRAS, 177, 257
Pulone, L. 1992, Mem. Soc. Astron. Italiana, 63, 485
Reid, I. N. 1997, AJ, 114, 161
———. 1998, AJ, 115, 204
Renzini, A., et al. 1996, ApJ, 465, L23
Renzini, A., & Fusi Pecci, F. 1988, ARA&A, 26, 199
Rood, R. T. 1973, ApJ, 184, 815
Rood, R. T., & Crocker, D. A. 1985, in Horizontal-Branch and UV-bright Stars, ed. A. G. D. Philip (Schenectady: L. Davis), 99
Rood, R. T., & Crocker, D. A. 1989, in IAU Colloq. 111, The Use of Pulsating Stars in Fundamental Problems of Astronomy, ed. E. G. Schmidt (Cambridge: Cambridge Univ. Press), 103
Rood, R. T., Whitney, J., & D'Cruz, N. 1997, in Advances in Stellar Evolution, ed. R. T. Rood & A. Renzini (Cambridge: Cambridge Univ. Press), 74
Rutledge, G. A., Hesser, J. E., & Stetson, P. B. 1997, PASP, 109, 907 (RHS97)
Salaris, M., & Cassisi, S. 1996, A&A, 305, 858
Salaris, M., Chieffi, A., & Straniero, O. 1993, ApJ, 414, 580
Samus, N., Ipatov, A., Smirnov, O., Kravtsov, V., Alcaino, G., Liller, W., & Alvarado, F. 1995, A&AS, 112, 439
Sandage, A., & Smith, L. L. 1966, ApJ, 144, 886
Sandage, A., & Wallerstein, G. 1960, ApJ, 131, 598
Sandage, A. R., & Walker, M. F. 1955, AJ, 60, 230
Sarajedini, A. 1994a, PASP, 106, 404
———. 1994b, AJ, 107, 618
Sarajedini, A., & Forrester, W. L. 1995, AJ, 109, 1112
Sarajedini A., & Layden, A. 1997, AJ, 113, 264 (SL97)
Sarajedini, A., & Milone, A. A. E. 1995, AJ, 109, 269
Sarajedini, A., & Norris, J. E. 1994, ApJS, 93, 161 (SN94)
Straniero, O. 1988, A&AS, 76, 157
Straniero, O., Chieffi, A., & Limongi, M. 1997, ApJ, 490, 425 (SCL97)
Straniero, O., Chieffi, A., & Salaris, M. 1992, Mem. Soc. Astron. Italiana, 63, 315
Thomas, H. C. 1967, Z. Astrophys., 67, 420
VandenBerg, D. A., Stetson, P. B., & Bolte, M. 1996, ARA&A, 34, 461
Walker, A. R. 1990, AJ, 100, 1532
———. 1992a, AJ, 104, 1395
———. 1992b, PASP, 104, 1063
———. 1994, AJ, 108, 555
Whitney, J. H., et al. 1998, ApJ, 495, 284
Zhao, G., & Magain, P. 1990, A&A, 238, 242
Zinn, R. 1980, ApJS, 42, 19
———. 1985, ApJ, 293, 424 (Z85)
Zinn, R., & West, M. J. 1984, ApJS, 55, 45